

Probing Gravitational-Wave Four-Point Correlators

Martina Ciprini ^{*}, Maria Lucia Marcelli [†], Gianmassimo Tasinato [‡]

*Physics Department, Swansea University, SA2 8PP, UK,
Dipartimento di Fisica e Astronomia, Università di Bologna,
INFN, Sezione di Bologna, viale B. Pichat 6/2, 40127 Bologna, Italy*

Abstract

Stochastic gravitational-wave backgrounds (SGWBs) of primordial origin offer a powerful probe of early-Universe physics and possible dark-sector dynamics. While most searches focus on the GW power spectrum, additional information is encoded in higher-order correlators that characterize the statistical properties of the signal. In this work we study non-Gaussian features of a cosmological SGWB generated at second order by vector fluctuations, a class of sources well motivated in early-Universe scenarios. Within this framework we develop tools to characterize higher-order GW correlators and compute representative four-point functions that generate a connected contribution to the GW trispectrum. We show that the trispectrum amplitude scales as the square of the GW power spectrum and peaks in characteristic folded momentum configurations, reflecting the structure of the nonlinear source. We then explore the observational implications. First, we demonstrate that the connected trispectrum contributes to the variance of two-point overlap reduction functions, including the Hellings–Downs curve relevant for pulsar timing arrays. We then construct the optimal estimator to measure the connected trispectrum with ground-based interferometers. Our results highlight how non-Gaussian SGWB statistics provide a complementary observable to probe the origin of GW backgrounds and to distinguish cosmological from astrophysical sources.

1 Introduction and Conclusions

The search for a stochastic gravitational-wave background (SGWB) of primordial origin offers a unique and powerful probe of the physics of the early Universe [1]. Unlike electromagnetic radiation, gravitational waves propagate essentially unimpeded from their production epoch, allowing them to carry direct information about physical processes occurring at extremely high energies and very early times. A particularly compelling target consists of scenarios in which present-day cosmic puzzles are explained through dynamics in the early Universe. Examples include models where primordial black holes account for a fraction of the dark matter, scenarios in which primordial vector fields seed the large-scale magnetic fields observed in galaxies and clusters, or frameworks in which dark matter arises from a dark photon sector. See, for example, [2–4] for reviews of these possibilities. These scenarios typically involve the amplification of primordial fluctuations or the dynamics of additional fields in the early Universe. As a generic consequence of their non-linear evolution, they inevitably source gravitational waves at second order in perturbations, leading to the production of a stochastic gravitational-wave background. In this sense,

^{*}martina.ciprini@studio.unibo.it

[†]marialucia.marcelli@studio.unibo.it

[‡]g.tasinato2208.at@gmail.com

the SGWB constitutes an unavoidable byproduct of the mechanisms responsible for generating the underlying cosmological structures or dark-sector components. See, e.g., [5, 6] and references therein. Importantly, the resulting SGWB signals are expected to display distinctive spectral and statistical properties that encode information about their production mechanisms. Characterizing these features therefore provides a powerful avenue to discriminate between different early-Universe scenarios and to probe the physics of the dark sector.

A central challenge in the context of SGWB physics is the identification of observables capable of discriminating among different gravitational-wave sources, whether primordial [1] or astrophysical [7], and of accurately extracting their physical properties. Several strategies have been proposed to distinguish cosmological from astrophysical SGWB, including the study of their spectral profiles (see e.g. [1, 8–10] and references therein) and of their anisotropies: see e.g. [11–14].

In this work we investigate primordial non-Gaussian features in the distribution of gravitational waves as potential observables for discriminating among different sources of the SGWB. Non-Gaussianity has long been recognized as a powerful probe of early-Universe physics. In particular, primordial non-Gaussianities generated during inflation have been extensively studied in the scalar sector of curvature perturbations (see e.g. [15]), and constraints of their amplitude and shape in the cosmic microwave background have played a crucial role in ruling out classes of inflationary models [16, 17]. In comparison, much less attention has been devoted to the study of primordial non-Gaussianity in SGWBs of cosmological origin, and to the development of suitable estimators to detect such signals with gravitational-wave experiments. Our work aims to contribute to this direction. We focus on the class of dark-sector scenarios discussed above, in which gravitational waves are generated at second order in fluctuations. Since the GW signal arises from non-linear sources, the resulting SGWB is expected to exhibit intrinsically non-Gaussian statistics. This property provides an additional observable that can be exploited to discriminate among different GW production mechanisms. In this work we therefore investigate primordial SGWB non-Gaussianity generated at second order in dark-sector models, and assess its potential as a diagnostic of the underlying early-Universe dynamics. We show how non-Gaussian features encode information about the physical processes responsible for GW production, and we discuss the prospects for detecting such signatures with present and future gravitational-wave experiments. Our analysis aims to bridge a gap between theoretical predictions and observational strategies, exploring small-scale SGWB non-Gaussianities by working at the interface between gravitational-wave theory and experimental searches.

Astrophysical SGWBs, being generated by the cumulative contribution of a large number of independent sources, are expected to be nearly Gaussian by virtue of the central limit theorem [18, 19]. This expectation holds provided that a sufficiently large population of sources contributes to the signal. An important exception arises when the SGWB is produced by a limited number of unresolved sources. In this regime the signal can exhibit a so-called “popcorn” character, reflecting the Poissonian statistics of the underlying astrophysical events. The resulting background is then characterized by a distinct form of non-Gaussianity associated with the discreteness of the sources. The search for and characterization of such signals is an active area of research; see, for example, [19–30]. See also [31, 32] for comprehensive reviews.

Cosmological gravitational-wave backgrounds, by contrast, originate from processes operating in the early Universe and can exhibit coherence over very large scales. As a consequence, they may

possess non-vanishing higher-order correlators with statistical properties that differ qualitatively from the Poisson-type non-Gaussianities expected in astrophysical backgrounds. Non-Gaussian features in the SGWB therefore constitute a potentially powerful observable for distinguishing among different classes of GW sources. Symmetry arguments and specific model-building approaches are known to provide powerful constraints on the possible shapes and properties of cosmological GW non-Gaussianities (see, e.g., [33–41]). Here we show that features of a family of induced GW sources allow us to accurately characterize the structure of observable non-Gaussian GW correlators, and to investigate their specific observational consequences.

We focus on SGWBs induced at second order by vector fluctuations, see e.g. [42–50]. These constitute the vector-field analogue of the well-studied case of scalar-induced SGWBs, extensively investigated in primordial black hole scenarios, starting from [51–57]. This setup, described in Section 2, provides a useful benchmark scenario, as it leads to technically simpler and physically transparent calculations of GW correlators. In particular, time and momentum integrations factorize within the relevant convolution integrals, allowing the time integrals to be performed analytically. This procedure isolates characteristic non-Gaussian quadrilateral shapes for the Fourier momenta, associated with *folded* configurations, and they naturally leads to the notion of *stationary non-Gaussianity* [58, 59]. We extend this framework by carrying out in Section 3 an analytic study of representative GW four-point functions, which generate a connected contribution to the GW trispectrum. (We do not consider spin-2 GW three-point functions, since they are not detectable with pulsar timing arrays or ground-based interferometers, see e.g. [60].) We show that the amplitude of the GW trispectrum scales as the square of the GW power spectrum.

In Section 4 we then investigate the observational implications of these results, demonstrating that the connected trispectrum can contribute to the variance of two-point overlap reduction functions – most notably to the variance of the Hellings–Downs curve relevant for pulsar timing array experiments. Finally, we analytically compute the four-point overlap reduction functions for ground-based interferometers and construct the corresponding optimal estimator for their detection.

We hope that our findings will contribute to advancing the theoretical understanding of gravitational-wave non-Gaussianities in well-motivated early-Universe scenarios, while also helping to identify robust observational signatures that could be probed by current and future gravitational-wave experiments.

2 Our set-up, and the SGWB two-point function

We study gravitational waves (GW) produced during the era of radiation domination, induced at second order in perturbations by primordial magnetic field fluctuations generated during cosmic inflation. Such magnetic fields can be associated with Standard Model electromagnetism and primordial magnetogenesis [3], or they can represent the magnetic-field components of dark vector models aimed at describing dark matter via longitudinal massive vector dynamics (see e.g. [61]). In our work, we consider a vector-induced SGWB as benchmark scenario for the broad family of models able to produce a background of GW at second order in fluctuations. In this and the next section we compute two-point and non-Gaussian correlators respectively. We show that our

set-up offers advantages with respect to the scalar-induced case, leading to technically feasible and physically transparent calculations. Then, in Section 4, we analyse how GW non-Gaussianities can offer new handles to probe or constrain properties of dark sector physics with GW experiments.

An example of vector field models from the early universe. Scenarios involving vector fields produced in the primordial universe arise in different contexts. To consider a concrete example, one of the simplest models of magnetogenesis from cosmic inflation is based on the Ratra action for the vector sector [62]

$$S = -\frac{1}{4} \int d^4x \sqrt{-g} f(\phi) F_{\mu\nu} F^{\mu\nu}, \quad (2.1)$$

where $F_{\mu\nu} = \partial_\mu A_\nu - \partial_\nu A_\mu$ is the vector field strength, and $f(\phi)$ a function of the inflaton field and its gradient, which characterise the dynamics of the vector. We work in the mostly-plus metric convention. We assume a Friedmann–Robertson–Walker background metric with scale factor $a(\tau)$, with τ denoting the conformal time. We focus on the magnetic part of the vector spectrum only. We decompose the magnetic field in Fourier modes as

$$\begin{aligned} B_i(\tau, \mathbf{x}) &= \int \frac{d^3\mathbf{k}}{(2\pi)^3} e^{i\mathbf{k}\cdot\mathbf{x}} B_i(\tau, \mathbf{k}) \\ &= \sum_\lambda \int \frac{d^3\mathbf{k}}{(2\pi)^3} e^{i\mathbf{k}\cdot\mathbf{x}} e_i^{(\lambda)}(\hat{k}) B_{\mathbf{k}}(\tau), \end{aligned} \quad (2.2)$$

The spin-one polarization tensors $e_i^{(\lambda)}(\hat{k})$ are defined in circular basis with helicity $\lambda = R/L = \pm 1$. They are constructed from two orthonormal unit vectors \hat{p} and \hat{q} , transverse to the direction \hat{k}

$$e_i^{(\lambda)}(\hat{k}) = \frac{\hat{p}_i + i\lambda \hat{q}_i}{\sqrt{2}}. \quad (2.3)$$

Hatted vectors denote unit vectors, e.g. $\hat{k} = \mathbf{k}/k$ with $k = |\mathbf{k}|$. We assume that inflationary dynamics generate a magnetic-field spectrum characterized by the following two-point function in Fourier space

$$\langle B_i(\tau, \mathbf{k}) B_j^*(\tau, \mathbf{q}) \rangle = (2\pi)^3 \delta(\mathbf{k} - \mathbf{q}) \langle B_i(\tau, \mathbf{k}) B_j^*(\tau, \mathbf{k}) \rangle_\Delta, \quad (2.4)$$

where

$$\langle B_i(\tau, \mathbf{k}) B_j^*(\tau, \mathbf{k}) \rangle_\Delta = \pi_{ij}(\hat{k}) P_B(k). \quad (2.5)$$

The Dirac-delta in Fourier momenta appearing in Eq. (2.4) is associated with the rotational invariance of the background. The index Δ in $\langle \dots \rangle_\Delta$ denotes correlators factorising the aforementioned delta function.

The tensor π_{ij} is a combination of spin-1 polarization tensors

$$\pi_{ij}(\hat{k}) = \sum_{\lambda=\pm 1} e_i^{(\lambda)}(\hat{k}) e_j^{(\lambda)*}(\hat{k}) = \delta_{ij} - \hat{k}_i \hat{k}_j, \quad (2.6)$$

For convenience we define the rescaled magnetic field spectrum $\mathcal{P}_B(k)$ through the formula

$$P_B(k) \equiv \langle B_{\mathbf{k}}(\tau) B_{\mathbf{k}}^*(\tau) \rangle_{\Delta} = \frac{2\pi^2}{k^3} \mathcal{P}_B(k). \quad (2.7)$$

The explicit scale dependence of the function $\mathcal{P}_B(k)$ depends on the set-up one considers – the model of inflation, and the structure of the function f in the specific model of Eq. (2.1). See e.g. [3] for a review. Besides couplings as Eq. (2.1), one can also consider models of massive vectors during inflation, with interesting consequences for the dark matter problem [61]. In all these cases the magnetic field spectrum can get enhanced at small scales, and our considerations in principle apply to all these scenarios. We shall assume though that vector perturbations propagate around a system with a vanishing vector field background, so that spin-1 fluctuations have Gaussian statistics – although, as we shall learn, they can lead to non-Gaussianities in the induced spin-2, GW background.

Computation of the induced SGWB spectrum An enhanced magnetic field spectrum $\mathcal{P}_B(k)$ at small scales can source a background of GW at second order in fluctuations, after inflation ends. In this Section we focus on two-point correlation functions and compute the induced GW spectrum, while in Section 3 we discuss SGWB non-Gaussianities.

We decompose tensor perturbations corresponding to GW as

$$h_{ij}(\tau, \mathbf{x}) = \sum_{\lambda} \int \frac{d^3\mathbf{k}}{(2\pi)^3} e^{i\mathbf{k}\cdot\mathbf{x}} e_{ij}^{(\lambda)}(\hat{k}) h_{\mathbf{k}}^{(\lambda)}(\tau), \quad (2.8)$$

where $e_{ij}^{(\lambda)}(\hat{k})$ are the spin-2, transverse–traceless (TT) polarization tensors in circular basis $(R, L) = \pm 2$ ¹. The spin-2 polarization tensors are built as product of spin-1 ones of Eq. (2.3):

$$e_{ij}^{(\lambda)}(\hat{k}) = e_i^{(\lambda)}(\hat{k}) e_j^{(\lambda)}(\hat{k}). \quad (2.10)$$

The following combination of spin-2 polarization tensors defines the projector operator, an important quantity in our analysis:

$$\begin{aligned} \Lambda_{ij\ell m} &= \sum_{\lambda=\pm 2} e_{ij}^{(\lambda)} e_{\ell m}^{(\lambda)*} \\ &= e_{ij}^{(L)} e_{\ell m}^{(L)*} + e_{ij}^{(R)} e_{\ell m}^{(R)*} = e_{ij}^{(+)} e_{\ell m}^{(+)} + e_{ij}^{(\times)} e_{\ell m}^{(\times)} \\ &= \frac{1}{2} \left(\pi_{i\ell} \pi_{jm} + \pi_{j\ell} \pi_{im} - \pi_{ij} \pi_{\ell m} \right). \end{aligned} \quad (2.11)$$

which projects a two-index tensor in its transverse-traceless components.

In order to ensure that $h_{ij}(\tau, \mathbf{x})$ is real, we assume $h_{\mathbf{k}}^{(\lambda)*}(\tau) = h_{-\mathbf{k}}^{(-\lambda)}(\tau)$. The two-point

¹The spin-2 polarization tensors in circular basis $(R, L) = (+2, -2)$ are related to the ones in $(+, \times)$ basis by the formula

$$e_{ij}^{(\pm 2)}(\hat{k}) = \frac{e_{ij}^{(+)}(\hat{k}) \pm i e_{ij}^{(\times)}(\hat{k})}{\sqrt{2}}. \quad (2.9)$$

We assume that the polarization tensors $e_{ij}^{(+, \times)}$ are real, hence $\left(e_{ij}^{(\pm 2)} \right)^* = e_{ij}^{(\mp 2)}$.

correlators for Fourier components satisfy the condition

$$\langle h_{\mathbf{k}}^{(\lambda_1)}(\tau) h_{\mathbf{q}}^{(\lambda_2)*}(\tau) \rangle = (2\pi)^3 \delta^{(3)}(\mathbf{k} - \mathbf{q}) \delta_{\lambda_1, \lambda_2} \langle h_{\mathbf{k}}^{(\lambda_1)}(\tau) h_{\mathbf{k}}^{(\lambda_1)*}(\tau) \rangle_{\Delta}. \quad (2.12)$$

The role of the δ -function over momenta has been discussed earlier. Here, the Kronecker δ -function in the polarization indexes is related to the conservation of helicity for the spin-2 massless modes ². Using the previous Fourier decomposition, we define the tensor power spectrum as

$$\mathcal{P}_h(k) = \frac{k^3}{4\pi^2} \sum_{\lambda} \langle h_{\mathbf{k}}^{(\lambda)}(\tau) h_{\mathbf{k}}^{(\lambda)*}(\tau) \rangle_{\Delta}. \quad (2.13)$$

This is the quantity we wish to compute in this Section, reviewing and in part extending results developed e.g. in [50, 63].

Given an early universe model producing magnetic fields, our computation of the second order, induced GW spectrum follows [50]. After inflation ends, for $\tau \geq \tau_f$, the GW Fourier mode functions obey

$$h_{\mathbf{k}}^{(\lambda)''}(\tau) + 2\mathcal{H} h_{\mathbf{k}}^{(\lambda)'}(\tau) + k^2 h_{\mathbf{k}}^{(\lambda)}(\tau) = S^{(\lambda)}(\tau, \mathbf{k}), \quad (2.14)$$

where primes indicate derivative along conformal time, $\mathcal{H} = a'/a$, and the source term on the right-hand-side of this equation is induced by the anisotropic stress associated with magnetic fields. It reads

$$\begin{aligned} S^{(\lambda)}(\tau, \mathbf{k}) &= \frac{2}{a^2(\tau)} e^{(\lambda)ij}(\hat{k}) \Lambda_{ij}{}^{mn}(\hat{k}) \tau_{mn}^{(B)}(\mathbf{k}) \\ &= \frac{2}{a^2(\tau)} e^{(\lambda)ij}(\hat{k}) \tau_{ij}^{(B)}(\mathbf{k}). \end{aligned} \quad (2.15)$$

The magnetic-field stress tensor in Eq.(2.15) is given by (see e.g. [44])

$$\tau_{ij}^{(B)}(\mathbf{k}) = \frac{1}{4\pi} \int \frac{d^3\mathbf{p}}{(2\pi)^3} \left[B_i(\mathbf{p}) B_j(\mathbf{k} - \mathbf{p}) - \frac{\delta_{ij}}{2} B_m(\mathbf{p}) B_m(\mathbf{k} - \mathbf{p}) \right]. \quad (2.16)$$

Since $\Lambda_{ii}{}^{\ell m} = \Lambda_{ij}{}^{\ell \ell} = 0$, the term proportional to δ_{ij} in the previous expression does not contribute once contracted with the projector Λ . The formal solution of Eq. (2.14) can be written as

$$h_{\mathbf{k}}^{(\lambda)}(\tau) = \frac{1}{a(\tau)} \int d\tau' g_k(\tau, \tau') a(\tau') S^{(\lambda)}(\tau', \mathbf{k}), \quad (2.17)$$

where during radiation domination (RD) the Green function is

$$g_k(\tau, \tau') = \frac{1}{k} \sin [k (\tau - \tau')]. \quad (2.18)$$

As in [43], we parameterize the scale factor at late times during this epoch as

$$a(\tau) = H_0 \sqrt{\Omega_{\text{rd}}} \tau, \quad (2.19)$$

²This is an important point on which we return again in Section 3 when discussing non-Gaussian correlators.

with H_0 the present-day Hubble parameter, and $\Omega_{\text{rd}} = \frac{\rho_{\text{rad}}}{\rho_{\text{cr}}}$ the radiation density parameter. The tensor power spectrum defined in Eq. (2.13) results

$$\mathcal{P}_h(k) = \frac{k^3}{4\pi^2 a^2(\tau)} \int d\tau_1 d\tau_2 g_k(\tau, \tau_1) g_k(\tau, \tau_2) a(\tau_1) a(\tau_2) \left(\sum_{\lambda} \langle S^{(\lambda)}(\tau_1, \mathbf{k}) S^{(\lambda)*}(\tau_2, \mathbf{k}) \rangle_{\Delta} \right). \quad (2.20)$$

Using Eq. (2.16) and Wick theorem, the source two-point correlator summed over helicities becomes

$$\begin{aligned} \sum_{\lambda} \langle S_{\mathbf{k}}^{(\lambda)}(\tau_1) S_{\mathbf{k}}^{(\lambda)*}(\tau_2) \rangle_{\Delta} &= \frac{4}{(4\pi)^2 a^2(\tau_1) a^2(\tau_2)} \int d^3 p \Lambda_{ij}^{\ell n}(\hat{\mathbf{k}}) [\pi^i_{\ell}(\hat{\mathbf{p}}) \pi^j_n(\hat{\mathbf{n}}) + \pi^i_n(\hat{\mathbf{p}}) \pi^j_{\ell}(\hat{\mathbf{n}})] \\ &\quad \times P_B(p) P_B(|\mathbf{k} - \mathbf{p}|), \end{aligned} \quad (2.21)$$

where $\hat{\mathbf{n}} = (\mathbf{k} - \mathbf{p})/|\mathbf{k} - \mathbf{p}|$, and we used the definition (2.4) for the magnetic field power spectrum. Non-Gaussian connected contributions are neglected, since as explained above we consider set-up of Gaussian vector fields only. Following [54, 57], we introduce the variables

$$u = \frac{|\mathbf{k} - \mathbf{p}|}{k}, \quad v = \frac{p}{k}, \quad \mu = \frac{\mathbf{k} \cdot \mathbf{p}}{kp} = \frac{1 - u^2 + v^2}{2v}. \quad (2.22)$$

Contracting the tensor structure above (see e.g. [64]) one finds

$$\begin{aligned} \mathcal{C}_0(u, v) &= \Lambda_{ij}^{\ell n}(\hat{\mathbf{k}}) [\pi^i_{\ell}(\hat{\mathbf{p}}) \pi^j_n(\hat{\mathbf{n}}) + \pi^i_n(\hat{\mathbf{p}}) \pi^j_{\ell}(\hat{\mathbf{n}})] \\ &= (1 + \mu^2) \left(1 + \frac{(1 - \mu v)^2}{u^2} \right). \end{aligned} \quad (2.23)$$

Using $d^3 p = 2\pi k^3 v^2 dv d\mu$, we obtain – in terms of the rescaled magnetic field spectrum \mathcal{P}_B of Eq. (2.7):

$$\sum_{\lambda} \langle S_{\mathbf{k}}^{(\lambda)}(\tau_1) S_{\mathbf{k}}^{(\lambda)*}(\tau_2) \rangle_{\Delta} = \frac{2\pi^3}{k^3 a^2(\tau_1) a^2(\tau_2)} \int_0^{\infty} \frac{dv}{u^3 v} \int_{-1}^1 d\mu \mathcal{P}_B(ku) \mathcal{P}_B(kv) \mathcal{C}_0(u, v). \quad (2.24)$$

Substituting Eq. (2.24) into Eq. (2.20), the tensor spectrum \mathcal{P}_h defined in Eq. (2.20) factorizes in two pieces as

$$\mathcal{P}_h(\tau, k) = \frac{\pi}{2a^2(\tau)} \mathcal{I}_{\tau}^2 \mathcal{I}_B, \quad (2.25)$$

with

$$\mathcal{I}_{\tau}^2 = \left(\int_{\tau_R}^{\tau} d\tau_1 \frac{g_k(\tau, \tau_1)}{a(\tau_1)} \right)^2, \quad (2.26)$$

$$\mathcal{I}_B = \int_0^{\infty} \frac{dv}{u^3 v} \int_{-1}^1 d\mu \mathcal{P}_B(ku) \mathcal{P}_B(kv) \mathcal{C}_0(u, v). \quad (2.27)$$

It is important to emphasize that the expression in Eq. (2.25) exhibits a *factorizable* structure in its time and momentum integrations. As a consequence, the time integral is easily tractable and can be carried out analytically. This property will play a central role in our analysis of higher-order correlators in the next section. It considerably streamlines the computations and yields physically transparent results, particularly in clarifying which momentum configurations and non-Gaussian shapes are permitted for n -point functions within the setup under consideration.

The time integral (2.26) is independent from the magnetic field source – it controls the effects of propagation during RD. Instead, the momentum integral \mathcal{I}_B of Eq. (2.27) is time independent during RD – while it depends on the primordial magnetic field spectrum \mathcal{P}_B . During radiation domination, $a(\tau)/a(\tau_1) = \tau/\tau_1$ and $aH = 1/\tau$: see Eq. (2.19). Averaging over rapid oscillations, and taking the large τ limit within radiation domination, yields for the time integral

$$\bar{\mathcal{I}}_\tau^2 = \frac{1}{2k^2 H_0^2 \Omega_R} \left[\text{Ci}^2(|k\tau_R|) + \left(\frac{\pi}{2} - \text{Si}(|k\tau_R|) \right)^2 \right]. \quad (2.28)$$

with Ci and Si respectively the cosine and sine integral functions, and the bar over $\bar{\mathcal{I}}$ indicates average over rapid oscillations. We used the fact that in RD $a^2 H = H_0 \sqrt{\Omega_R}$. Hence the time integral \mathcal{I}_τ^2 becomes independent from time for τ sufficiently large in RD. The quantity within square parenthesis in Eq. (2.28) has a mild, logarithmic dependence on momenta in the limit of small $|k\tau_f|$. See also [50] and references therein. Having introduced the averaged time integral, we define the averaged power spectrum as

$$\bar{\mathcal{P}}_h \equiv \frac{1}{2} \frac{\pi}{2a^2(\tau)} \bar{\mathcal{I}}_\tau^2 \mathcal{I}_B. \quad (2.29)$$

We plug (2.28) in Eq. (2.25), and evaluate the scale factor at time τ when the mode of momentum k crosses the horizon during RD: $a^2(\tau_k) = \Omega_R H_0^2 / k^2$, finding

$$\bar{\mathcal{P}}_h(\tau_k, k) = \frac{\pi}{8\Omega_R^2 H_0^4} \left[\text{Ci}^2(|k\tau_R|) + \left(\frac{\pi}{2} - \text{Si}(|k\tau_R|) \right)^2 \right] \mathcal{I}_B. \quad (2.30)$$

In order to take into account of the GW redshift from horizon crossing to today, we include effects of transfer function to the previous formulas, amounting to the inclusion of an overall factor of $a^2(\tau_k)/2$ (see e.g. [65]), hence today we have

$$\bar{\mathcal{P}}_h(k) = \frac{\pi}{16\Omega_R H_0^2 k^2} \left[\text{Ci}^2(|k\tau_R|) + \left(\frac{\pi}{2} - \text{Si}(|k\tau_R|) \right)^2 \right] \mathcal{I}_B. \quad (2.31)$$

Explicit examples. We are now left with the computation of \mathcal{I}_B in Eq.(2.27) – which is the quantity that depends on \mathcal{P}_B . We *do not* limit our attention to power-law profiles for the vector spectrum \mathcal{P}_B , as often considered, and we instead allow for richer momentum dependences, motivated by recent advances in inflationary model buildings including non-slow-roll phases (see e.g. [50,63] for models of primordial magnetogenesis including the effects of such phases). We keep the discussion broad without focussing on explicit model building. Instead we consider general, simple templates with a peak in the magnetic field spectrum.

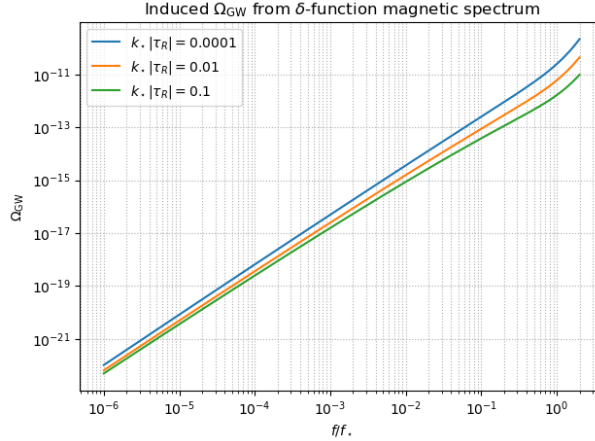


Figure 1: The GW energy spectrum Ω_{GW} associated a monochromatic (delta-function) magnetic power spectrum, plotted as a function of f/f_* for different values of $k_*|\tau_R|$. See Eq. (2.37). Notice that the the spectrum drops to zero for $f/f_* \geq 2$.

As a first example, we focus on the case of delta-like magnetic spectrum, which can be motivated by models of inflation with ultra-slow-roll phases able to produce sharp peaks in the spectrum

$$\mathcal{P}_B(k) = A_B \delta(\ln[k/k_*]) , \quad (2.32)$$

with k_* a characteristic scale indicating the epoch during inflation when departures from slowroll occur. A scenario with such sharp peaks is not easy to realize in practice, but this set-up has the advantage of being analytically tractable. In fact, changing variables as $u = (t + s + 1)/2$, $v = (t - s + 1)/2$, the integral \mathcal{I}_B containing delta-functions can be explicitly evaluated, giving

$$\mathcal{I}_B(k) = \int_0^\infty dt \int_{-1}^1 ds (1-s+t)^{-2} (1+s+t)^{-2} \mathcal{P}_B(ku) \mathcal{P}_B(kv) \mathcal{C}_0(t, s). \quad (2.33)$$

$$= A_B^2 \frac{k^2 (k^2 + 4k_*^2)^2}{128 k_*^6} \Theta(2k_* - k). \quad (2.34)$$

Hence the final expression for the GW spectrum is

$$\bar{\mathcal{P}}_h(\tau_0, k) = \left(\frac{\pi A_B^2}{128 k_*^2 H_0^2 \Omega_R} \right) \left(1 + \frac{k^2}{4k_*^2} \right)^2 \left[\text{Ci}^2(|k\tau_R|) + \left(\frac{\pi}{2} - \text{Si}(|k\tau_R|) \right)^2 \right] \Theta(2k_* - k). \quad (2.35)$$

This is an increasing function of k/k_* , dropping to zero for $k/k_* > 2$. As expected from the structure of the convolution integrals, its amplitude is proportional to the square of the amplitude of the magnetic field spectrum. Compare with Eq. (2.32). It is also convenient to compute the energy density in GW, given by

$$\Omega_{\text{GW}} \equiv \frac{1}{12} \left(\frac{k}{aH} \right)^2 \bar{\mathcal{P}}_h, \quad (2.36)$$

being this quantity usually considered in GW experiments aiming at characterising the SGWB

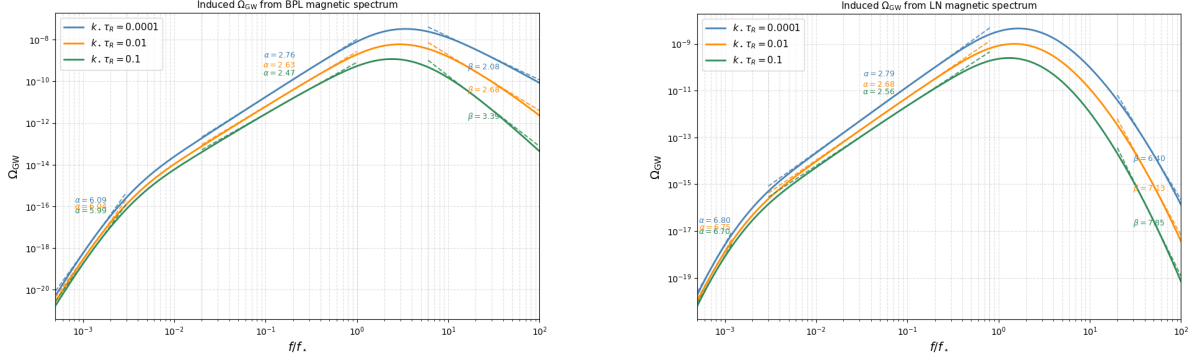


Figure 2: Profiles of Ω_{GW} as function of GW frequency over a characteristic scale f_* . **Left panel:** GW spectrum induced by a broken power law profile for the magnetic field, (2.38), choosing $n_1 = 4$, $n_2 = -2$, $\sigma = 1$. **Right panel:** GW spectrum associated to the log-normal profile of Eq. (2.39), with $\Delta = 0.8$. In both cases, $P_0 = 10^2$, and fix the quantity $|k_* \tau_R| = 10^{-2}$ in Eq.(2.31).

spectral shape. It is expressed in terms of GW frequency, $f/f_* = k/k_*$.

Plugging expression (2.35) into (2.36) we get the form of the full GWs energy spectrum

$$\Omega_{\text{GW}}(\tau_0, k) = \left(\frac{\pi A_B^2}{128 k_*^2 H_0^2 \Omega_R} \right) \left(\frac{k^2}{12 H_0^2} \right) \left(1 + \frac{k^2}{4 k_*^2} \right)^2 \left[\text{Ci}^2(|k \tau_R|) + \left(\frac{\pi}{2} - \text{Si}(|k \tau_R|) \right)^2 \right] \times \Theta(2k_* - k), \quad (2.37)$$

where we used $a(\tau_0) = 1$.

The plot of (2.37) as a function of $k/k_* = f/f_*$ for different values of $k_* \tau_R$ is shown in figure 1; we plot $\Omega_{\text{GW}}(f)$ since this is the usually considered quantity in GW experiments aiming at characterising the SGWB spectral shape. Since a δ -function source is physically hard to achieve, we only focus on the qualitative shape of the spectrum. Therefore, we set the overall normalization parameters to unity, as they only change the amplitude of the function but not the dependence of Ω_{GW} on k/k_* ; similarly, we fix $A_B = 10^{-6}$. In our setup we assume $k_* |\tau_R| \ll 1$, accordingly with the beyond-slow-roll magnetogenesis framework of [50], where $k_* \equiv -1/\tau_1$, τ_1 is the instant at which the non-slow-roll phase begins during inflation, and τ_R denotes the end of inflation. With this choice, the only relevant parameter controlling the time integral part is the dimensionless combination $k_* |\tau_R|$, which enters the argument of the oscillatory term through $k \tau_R = (k/k_*) (k_* \tau_R)$. For $k_* |\tau_R| \ll 1$ these oscillatory functions show a mild variation. As a result, in the monochromatic delta-function case the spectrum is essentially controlled by the monotonically increasing prefactor and exhibits a sharp cutoff at $k = 2k_*$. This qualitative behaviour is similar to the monochromatic delta-function template discussed in [46] in an analogous setup of GWs induced by primordial magnetic fields, where a monotonically increasing Ω_{GW} with a sharp cutoff at $k = 2k_*$ is likewise found.

After the previous analytical model, we can numerically handle two more realistic templates for the momentum profile of \mathcal{P}_B , which are frequently considered in the analog context of scalar

induced gravitational waves. First, a broken power-law (BPL) profile

$$\mathcal{P}_B(k) = P_0 \left(\frac{k}{k_\star} \right)^{n_1} \left(\frac{1}{2} + \frac{1}{2} \left(\frac{k}{k_\star} \right)^\sigma \right)^{\frac{n_2 - n_1}{\sigma}} \quad (2.38)$$

where P_0 an overall amplitude, k_\star is a pivot momentum scale, $n_{1,2}$ characterize the slopes of the power-laws on both sides of the break, and σ controls the smoothness of the break transition. Second, a log-normal (LN) spectrum

$$\mathcal{P}_B(k) = \frac{P_0}{\sqrt{2\pi}\Delta} e^{-(\ln k/k_\star)^2/(2\Delta^2)} \quad (2.39)$$

maximised at k_\star , where Δ controls the width of the peak. We perform numerically the momentum integrals \mathcal{I}_B , and represent in Fig 2 our results in terms of GW energy density of Eq. 2.36. Both the panels in Fig 2 have a similar profile, and we notice a rapid decay in power at $f > 2f_\star$, analogously to what found for the case of delta-like magnetic source. In both cases the GW spectrum exhibits the same qualitative structure: an infrared rise at $k/k_\star \ll 1$, a maximum at wavenumbers of order the characteristic scale k_\star , and a decay at larger wavenumbers. At small k the spectrum grows approximately as a power law,

$$\Omega_{\text{GW}}(k) \propto k^{\alpha(k)}, \quad (2.40)$$

with an effective slope $\alpha(k)$ that is not constant and progressively flattens as k/k_\star approaches 10^{-1} . Around the peak the slope crosses zero, while at larger k the spectrum decreases and can be described by a negative effective slope, $\Omega_{\text{GW}}(k) \propto k^{-\beta(k)}$. Figure 2 shows the resulting Ω_{GW} spectra for the two magnetic templates considered (BPL and LN), together with power-law fits performed over different frequency intervals. This procedure highlights how the effective slopes α and β vary across the integration ranges. The main difference between the two cases appears in the ultraviolet tail. For the BPL template the maximum occurs at k/k_\star of order a few and the subsequent decay is relatively mild, leaving an extended high- k tail consistent with a power-law behaviour. In contrast, for the LN template the peak lies closer to $k/k_\star \sim \mathcal{O}(1)$ and the ultraviolet suppression is significantly steeper, reflecting the stronger localization of the source spectrum around k_\star . Finally, varying $k_\star\tau_R$ mainly rescales the overall amplitude of the signal. In the range shown in the figure, increasing $|k_\star\tau_R|$ reduces the amplitude of Ω_{GW} , in agreement with the explicit dependence of the oscillatory functions on $|k\tau_R|$, as already observed in the δ -function case. Finite-width peaked source spectra are more realistic than the monochromatic approximation and naturally produce a GW signal peaking around $k \sim k_\star$. Moreover, they display infrared and ultraviolet behaviours that are qualitatively consistent with those commonly found in peaked-source SGWB scenarios in the literature, for instance in the case of scalar-induced gravitational waves (see e.g. [5] and references therein).

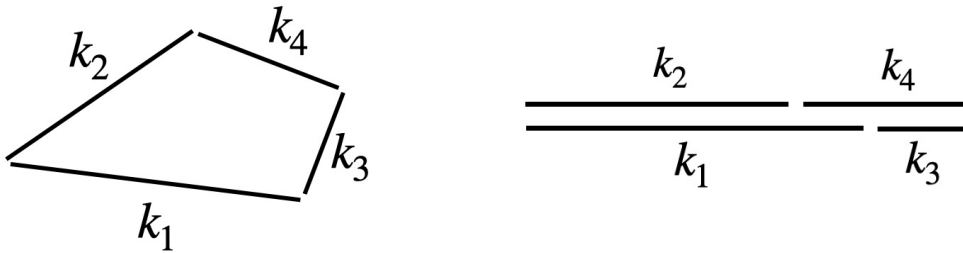


Figure 3: Graphical representation of the shapes of closed quadrilatera associated with the GW trispectrum. **Left panel:** a generic closed shape. **Right panel:** a flattened trispectrum shape, as the one we reduce to in our set-up. See main text for details.

3 Computation of induced GW non-Gaussianity

Definitions and motivations Since in our set-up the SGWB is sourced non-linearly in fluctuations by primordial vector fields, we expect that the corresponding connected higher order GW correlators are non-vanishing, and that they can lead to observational consequences for GW experiments. The physics of dark sector involving vector fields, as discussed above, offers distinctive connections between magnetogenesis [42–50], dark matter [66], and non-Gaussianities in the stochastic GW background. We aim to characterize the properties of the SGWB non-Gaussianities, with special emphasis on their implications for GW experiments which we explore in the next Section.

In this Section we demonstrate that the calculations carried on in Section 2 can be straightforwardly extended to study non-Gaussian GW correlators. Since three-point correlators of spin-2 GW associated with isotropic SGWB can *not* be directly detected with interferometer and pulsar timing array experiments (see e.g. [60]) we focus on four-point correlators, and study the so-called GW trispectrum. We show that the resulting trispectrum in our setup is stationary [58, 59] and assumes a folded shape in terms of its momenta.

We will be interested on the connected part of the GW four-point function, extracted from the combination of correlators in momentum space

$$\sum_{\lambda_i} \langle h_{\mathbf{k}_1}^{(\lambda_1)}(\tau) \left(h_{\mathbf{k}_2}^{(\lambda_2)}(\tau) \right)^* h_{\mathbf{k}_3}^{(\lambda_3)}(\tau) \left(h_{\mathbf{k}_4}^{(\lambda_4)}(\tau) \right)^* \rangle_{\Delta}, \quad (3.1)$$

where $\lambda_i = \pm 2$. In writing the previous equation we impose the momentum-conserving relation

$$\mathbf{k}_1 + \mathbf{k}_3 = \mathbf{k}_2 + \mathbf{k}_4 \quad (3.2)$$

associated with the rotational invariance of the background – hence the momenta \mathbf{k}_i form a closed quadrilaterum: see Fig 3, left panel. Moreover, as we are going to learn, in the set-up we consider the momenta \mathbf{k}_i actually lie all *aligned* along a common direction $\mathbf{k}_i = k_i \hat{n}$. See Fig 3, right panel for an example of momentum alignment.

Hence the set-up we consider leads to shapes corresponding to flattened quadrilateral configurations. Being the momenta of the massless spin-2 fields aligned, we impose the conservation of

total helicity in the correlators of Eq. (3.1). In Eq. (3.1) we then impose

$$\lambda_1 - \lambda_2 + \lambda_3 - \lambda_4 = 0 \quad (3.3)$$

where $\lambda_i = \pm 2 = (L, R)$. Hence the λ_i can assume the values $(LLLL)$, $(LLRR)$, $(LRRL)$, up to exchange of L with R . In this work, for definiteness, we assume that only the $(LLLL)$ and $(LLRR)$ are turned on (as well as the corresponding contributions with $L \leftrightarrow R$) and a sum over helicities reduce to

$$\sum_{\lambda_i} = \sum_{\lambda_{1,2}=\pm 2} . \quad (3.4)$$

We then define the trispectrum as

$$\mathcal{T}_h = \frac{1}{4} \frac{k_1^3 k_2^3 k_3^3}{(2\pi^2)^3} \sum_{\lambda_{1,2}=\pm 2} \langle h_{\mathbf{k}_1}^{(\lambda_1)}(\tau) \left(h_{\mathbf{k}_2}^{(\lambda_1)}(\tau) \right)^* h_{\mathbf{k}_3}^{(\lambda_2)}(\tau) \left(h_{\mathbf{k}_4}^{(\lambda_2)}(\tau) \right)^* \rangle_{\Delta}, \quad (3.5)$$

where k_i^3 overall factors are included to make the result dimensionless, in analogy with the power spectrum definition of Eq. (2.13). The structure of Eq. (3.5) automatically satisfies the condition (3.3).

From now on, we will be interested on the connected part of the trispectrum, which we still indicate with \mathcal{T}_h . For computing this quantity following Eq. (3.5), we start from the formal solution of the GW mode function given in Eq. (2.17). We proceed as in the previous section. The trispectrum \mathcal{T}_h defined in Eq.(3.5) results factorizable in a time and momentum integral as in Section 2:

$$\mathcal{T}_h = \frac{16}{a^4(\tau)} J_{\tau}(\tau) J_B(k_i) \quad (3.6)$$

with

$$J_{\tau}(\tau) = \prod_{i=1}^4 \int d\tau_i \frac{g_{k_i}(\tau, \tau_i)}{a(\tau_i)} \quad (3.7)$$

and

$$J_B(k_i) = \frac{1}{4} \frac{k_1^3 k_2^3 k_3^3}{(2\pi^2)^3} \mathcal{C}^{(B)}(\mathbf{k}_i), \quad (3.8)$$

with a polarization dependence as explained after Eq. (3.3) and where

$$\begin{aligned} \mathcal{C}^{(B)}(\mathbf{k}_i) = & \\ & \sum_{\lambda_{1,2}=\pm 2} \langle e^{(\lambda_1)ab}(\hat{k}_1) \tau_{ab}^{(B)}(\mathbf{k}_1) e^{(-\lambda_1)cd}(\hat{k}_2) \tau_{cd}^{(B)*}(\mathbf{k}_2) e^{(\lambda_2)ef}(\hat{k}_3) \tau_{ef}^{(B)}(\mathbf{k}_3) e^{(-\lambda_2)gh}(\hat{k}_4) \tau_{gh}^{(B)*}(\mathbf{k}_4) \rangle_{\Delta} \end{aligned} \quad (3.9)$$

We start with evaluating the time integral (3.7), which – as we are going to learn – is responsible for forcing the aforementioned condition of alignment on the directions \mathbf{k}_i .

The time integral in Eq. (3.7). We evaluate Eq. (3.7) in the limit of large observation time τ . Throughout, the Fourier momenta satisfy the closed-quadrilateral condition (3.2). The retarded Green function for each tensor mode is

$$g_{k_j}(\tau, \tau_j) = \frac{i}{2k_j} \left(e^{-ik_j(\tau-\tau_j)} - e^{ik_j(\tau-\tau_j)} \right). \quad (3.10)$$

Substituting Eq. (3.10) into Eq. (3.7) yields a sum of $2^4 = 16$ oscillatory contributions, each proportional to exponentials of the form $\prod_{j=1}^4 \exp[\pm ik_j \tau]$.

In the late-time limit $\tau \rightarrow \infty$, all terms are rapidly oscillating and hence suppressed – except for those for which the total phase is stationary. (Stationary phase approximation.) A direct inspection shows that stationarity is achieved if the *magnitudes* of the external momenta – and not only combinations with their directions as Eq. (3.2) – satisfy a relation of the form

$$\sum_{j=1}^4 s_j k_j = 0, \quad s_j = \pm 1. \quad (3.11)$$

Thus, configurations obeying the vectorial closure condition (3.2) contribute at late times only if they correspond to *flattened* or *folded* trispectrum shapes, in which the four sides are superimposed.³ See Fig. 3, right panel, as well as Appendix A for technical details.

In other words, in our setup the surviving contributions correspond to configurations in which the four momenta are collinear and aligned along a common direction $\hat{\mathbf{n}}$. Each momentum can then be parametrized as

$$\mathbf{k}_i = s_i k_i \hat{\mathbf{n}}, \quad s_i = \pm 1, \quad k_i > 0, \quad (3.12)$$

and the quadrilateral condition (3.2) reduces to a scalar constraint as Eq. (3.12):

$$s_1 k_1 + s_3 k_3 = s_2 k_2 + s_4 k_4. \quad (3.13)$$

See for example Fig.3, right panel, for an example where the $s_i = 1$ in the formula above.

We refer to this requirement as *stationarity* of the trispectrum, and stress that it is an unavoidable consequence of the structure of the time integrals in our framework. The stationary condition is essential for building observables detectable with GW experiments. Once this condition is satisfied, the decorrelation arguments of Refs. [67, 68] no longer apply, as discussed in [58, 59]. Indeed, the decoherence effects identified in [67, 68] typically arise from phase misalignment among waves produced in multiple causally disconnected regions; through the central limit theorem, this mechanism drives the signal toward Gaussianity. In contrast, the alignment condition in our setup enforces that the GW originate from the same direction, preventing such phase averaging. Our notion of *stationary GW non-Gaussianity* therefore singles out a distinct class of tensor non-Gaussian signatures with support in these aligned configurations.

Independently of this effect, [67, 68] show that gravitational waves may accumulate random phases during their propagation from source to detector, induced by long-wavelength energy-

³Another possibility arises when the quadrilateral has two pairs of parallel sides; we defer a discussion of this case to future work.

density fluctuations. These phases – physically associated with Shapiro time-delays – act on short-wavelength GW modes traveling over cosmological distances. As a result, they tend to suppress phase correlations in initially non-Gaussian fields, and they reduce the amplitude of connected tensor n -point functions for $n \geq 3$. Interestingly, in our case the unequal-time correlators depend on time differences only, thanks to the stationarity condition above (see e.g. [58]). Consequently, they are insensitive to the full propagation history of the waves and probe only the relatively short time scales relevant to the experiment.

Under the condition (3.12), the integral (3.7) can be evaluated straightforwardly (see Appendix A), but the result is cumbersome. For the simplest choice $s_i = 1$ in Eq. (3.13), and for equal $k_i = k$ (a special case relevant for the examples we consider) we find

$$\bar{J}_\tau = \frac{1}{8k^4 H_0^4 \Omega_R^2} \left[\text{Ci}^2(|k\tau_R|) + \left(\frac{\pi}{2} - \text{Si}(|k\tau_R|) \right)^2 \right]^2. \quad (3.14)$$

It is simply proportional to the square of the result we found for the two-point function case: compare with Eq. (2.28). Having introduced the averaged time integral \bar{J}_τ , we can accordingly define the averaged trispectrum, analogously as what we have done for the two-point function case

$$\bar{\mathcal{T}}_h(k_i) = \frac{1}{4} \frac{16}{a^4(\tau)} \bar{J}_\tau J_B(k_i). \quad (3.15)$$

The momentum integral of Eq. (3.8). We can now impose the collinearity condition of Eq. (3.12), and express the quantity $J_B(k_i)$ of Eq. (3.8) as (recall our choice of polarization indexes in the definition of trispectrum (3.5))

$$\begin{aligned} J_B(k_i) &= \frac{1}{4(4\pi)^4} \left(\frac{k_1^3 k_2^3 k_3^3}{(2\pi^2)^3} \right) K_{i_1 j_1 \dots i_4 j_4}(\mathbf{k}_i) \sum_{\lambda_{1,2}=\pm 2} e_{i_1 j_1}^{(\lambda_1)}(\hat{\mathbf{n}}) e_{i_2 j_2}^{(-\lambda_1)}(\hat{\mathbf{n}}) e_{i_3 j_3}^{(\lambda_2)}(\hat{\mathbf{n}}) e_{i_4 j_4}^{(-\lambda_2)}(\hat{\mathbf{n}}), \\ &= \frac{1}{4(4\pi)^4} \left(\frac{k_1^3 k_2^3 k_3^3}{(2\pi^2)^3} \right) K_{i_1 j_1 \dots i_4 j_4}(\mathbf{k}_i) \Lambda_{i_1 j_1 i_2 j_2} \Lambda_{i_3 j_3 i_4 j_4}, \end{aligned} \quad (3.16)$$

where we used the properties of combinations of polarization tensors – see Eq. (2.11). The eight-index tensor in Eq. (3.16), after defining $\mathbf{q}_a = k_a \hat{\mathbf{n}} - \mathbf{p}_a$, results

$$\begin{aligned} K_{i_1 j_1 \dots i_4 j_4}(\mathbf{k}_i) &= \int \prod_{a=1}^4 \frac{d^3 p_a}{(2\pi)^3} \\ &\left\langle B_{i_1}(\mathbf{p}_1) B_{j_1}(\mathbf{q}_1) B_{i_2}^*(\mathbf{p}_2) B_{j_2}^*(\mathbf{q}_2) B_{i_3}(\mathbf{p}_3) B_{j_3}(\mathbf{q}_3) B_{i_4}^*(\mathbf{p}_4) B_{j_4}^*(\mathbf{q}_4) \right\rangle. \end{aligned} \quad (3.17)$$

From this expansion, we are only interested in extracting the connected contributions, that correspond to the fully linked contractions in which all four source functions S_1, S_2^*, S_3, S_4^* are connected through magnetic field pairings. On the contrary, the disconnected contributions correspond to terms that factorize into products of lower-order point functions, like $\langle S_1 S_2^* \rangle \langle S_3 S_4^* \rangle$ or $\langle S_1 \rangle \langle S_2^* S_3 S_4^* \rangle$.

In order to isolate the connected part, we proceed as follows: we group the eight magnetic fields appearing in eq. (3.17) into four quadratic blocks, each block containing two magnetic

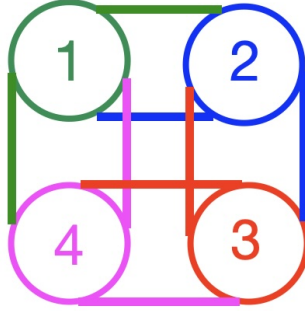


Figure 4: A particular lay-out for the four building blocks of magnetic fields leading to connected GW four-point functions, located on the vertexes of a square and linked by vector-field correlations. See main text for details.

Fourier modes, that we call legs. At vertex a we have the two legs $B_{i_a}(\mathbf{p}_a)$ and $B_{j_a}(\mathbf{q}_a)$, and analogously for the complex-conjugated blocks appearing in the second and fourth sources. A Wick contraction pairs any legs, irrespective of whether their indices originate from an i -slot or a j -slot of a given block. For instance, $B_{i_1}(\mathbf{p}_1)$ can contract with $B_{i_2}^*(\mathbf{p}_2)$ just as well as with $B_{j_2}^*(\mathbf{q}_2)$, and in the same way also two unconjugated modes can be connected, like $B_{i_1}(\mathbf{p}_1)$ and $B_{i_3}(\mathbf{p}_3)$. Recall that we can always pass from the conjugated to the non conjugated field by the relation $B_i(\mathbf{p})^* = B_i(-\mathbf{p})$. We can thus define the contraction between two modes as

$$\Pi_{lm} = B_l(\mathbf{k})B_m^*(\mathbf{k}') \Rightarrow \langle \Pi_{lm} \rangle = (2\pi)^3 \delta^{(3)}(\mathbf{k} - \mathbf{k}') P_B(k) \pi_{lm}(\hat{k}),$$

and analogously between two non-complex conjugated modes, with a $+$ inside the δ function. We now place the four source blocks (labelled by $a = 1, \dots, 4$) on the vertexes of a square, and represent each Wick contraction of magnetic modes as a line connecting two vertices (or better, two modes within two different vertices). Disconnected contributions correspond to configurations in which the graph factorizes into two (or more) independent subgraphs; these terms reduce to products of lower-order correlators and hence do not contribute to the connected four-point function. The connected contribution is obtained by retaining only those patterns that link all four vertices into a single closed loop. Therefore, there are six independent possibilities of connecting the blocks:

$$\langle \text{8pt function} \rangle_{\text{conn}} : \quad (1234) + (1243) + (1324) + (1342) + (1423) + (1432),$$

where the four numbers are the vertex labels a . For any of these six contributions, a specific contraction is obtained by assigning, at each vertex, which of its two legs is contracted to the next vertex along the cycle: for each of the six possibilities above, there are eight ways to contract magnetic Fourier modes among blocks.

For example, focusing on the option indicated as (1234), one of the eight possible diagrams

(the other choices lead to similar structures) is

$$\begin{aligned}
(1234)^1 &= \int \prod_{a=1}^4 \frac{d^3 p_a}{(2\pi)^3} \langle B_{i_1}(\mathbf{p}_1) B_{j_4}^\dagger(\mathbf{q}_4) \rangle \langle B_{j_1}(\mathbf{q}_1) B_{i_2}^\dagger(\mathbf{p}_2) \rangle \langle B_{j_2}^\dagger(\mathbf{q}_2) B_{i_3}(\mathbf{p}_3) \rangle \langle B_{j_3}(\mathbf{q}_3) B_{i_4}^\dagger(\mathbf{p}_4) \rangle \\
&= \delta[\hat{n}(k_3 - k_2 + k_1 - k_4)] \int d^3 p_1 P_B(p_1) P_B(k_1 - p_1) P_B(p_1 - k_1 + k_2) P_B(k_4 - p_1) \\
&\quad \times \pi_{i_1 j_4}(p_1) \pi_{i_2 j_1}(k_1 - p_1) \pi_{i_3 j_2}(p_1 - k_1 + k_2) \pi_{i_4 j_3}(k_4 - p_1), \tag{3.18}
\end{aligned}$$

where in the second equality we integrate over momenta $\mathbf{p}_{2,3,4}$, and for simplicity we understand the hats in the arguments of the π_{ij} tensors. For this specific contribution, the integral to compute for obtaining the corresponding part of J_B (see Eq. (3.16)) results

$$J_B^1 = \frac{(k_1 k_2 k_3)^3}{256\pi} \int \frac{dp d\mu}{p} C_1(k_i, p) \mathcal{P}_B(p) \frac{\mathcal{P}_B(k_1 - p)}{|k_1 - p|^3} \frac{\mathcal{P}_B(p - k_1 + k_2)}{|p - k_1 + k_2|^3} \frac{\mathcal{P}_B(k_4 - p)}{|k_4 - p|^3} \tag{3.19}$$

with

$$\mu \equiv \frac{\mathbf{k}_1 \cdot \mathbf{p}}{k_1 p}. \tag{3.20}$$

and

$$\begin{aligned}
C_1(k_i, p) &= \Lambda_{i_1 j_1 i_2 j_2}(n) \Lambda_{i_3 j_3 i_4 j_4}(n) \pi_{i_1 j_4}(p) \pi_{i_2 j_1}(k_1 - p) \\
&\quad \times \pi_{i_3 j_2}(p - k_1 + k_2) \pi_{i_4 j_3}(k_1 + k_3 - k_2 - p) \tag{3.21}
\end{aligned}$$

Notice that, since we integrate over all directions \hat{p} , the quantity J_B (hence the total trispectrum), results independent on the direction \hat{n} along which the momenta are aligned.

An explicit, simple example. So far, our results are general. As done in Section 2, for carrying on the integrals analytically we assume a delta-like source for the magnetic field spectrum

$$\mathcal{P}_B(k) = A_B \delta(\ln[k/k_\star]), \tag{3.22}$$

We introduce convenient variables

$$v \equiv \frac{p}{k_1}, \quad u \equiv \frac{|k_1 \hat{n} - \mathbf{p}|}{k_1}, \quad \sigma \equiv \frac{k_\star}{k_1}, \tag{3.23}$$

$$u_a \equiv \frac{|k_1 \hat{n} - k_2 \hat{n} - \mathbf{p}|}{k_1}, \quad u_b \equiv \frac{|k_4 \hat{n} - \mathbf{p}|}{k_1}, \tag{3.24}$$

so $\mu = (1 + v^2 - u^2)/(2v)$. Using the properties of Dirac delta function we can re-express the power spectra as

$$\mathcal{P}_B(p) = A_B \delta(\ln[p/k_\star]) = A_B \delta(\ln[v/\sigma]) = A_B \sigma \delta(v - \sigma), \tag{3.25}$$

and analog formulas apply to the remaining contributions to Eq. (3.19). Eq (3.19) can then be re-expressed as

$$J_B^1 = \frac{A_B^4}{256\pi} \left(\frac{k_2 k_3}{k_1^2} \right)^3 \int dv d\mu C_1(k_i, p) \delta(v - \sigma) \frac{\delta(u - \sigma)}{u^2} \frac{\delta(u_a - \sigma)}{u_a^2} \frac{\delta(u_b - \sigma)}{u_b^2} \quad (3.26)$$

In order for the delta-functions not to overconstrain the system, we select all sizes of the momenta to be equal, $k_i = k_1$ for $i = 2, 3, 4$, so that two of the delta-function conditions become redundant. The remaining delta-functions impose then $u = v = \sigma$, and $\mu = 1/(2\sigma)$. Under these conditions, the function C_1 in Eq. (3.21) reduces to

$$\begin{aligned} C_1 &= \frac{(1 + \mu^4)(2 - 4v\mu + v^2(1 + \mu^2))^2}{4(1 + v^2 - 2v\mu)} \\ &= \frac{1}{4} \left(1 + \frac{1}{4\sigma^2} \right)^2 \left(1 + \frac{1}{16\sigma^4} \right). \end{aligned} \quad (3.27)$$

The integral can then be easily evaluated giving

$$J_B^1 = \frac{A_B^4 k_1^6}{1024 \pi k_\star^6} \left(1 + \frac{k_1^2}{4k_\star^2} \right)^2 \left(1 + \frac{k_1^4}{16k_\star^4} \right) \Theta(2k_\star - k_1). \quad (3.28)$$

We can now assemble the previous result (3.28) with the time integral given in Eq. (3.14) (in our situation with all the k_i identical, as required by the delta-function conditions). The resulting contribution to the total trispectrum in radiation domination is given by Eq. (3.6): when evaluated today, we multiply the result by the transfer function coefficient $(a^2(\tau)/2)^2$. Hence, the result is a function of a single momentum scale k_1

$$\begin{aligned} \bar{\mathcal{T}}_h^1 &= \frac{A_B^4}{8192 \pi k_\star^4 H_0^4 \Omega_R^2} \left[\text{Ci}^2(|k_1 \tau_R|) + \left(\frac{\pi}{2} - \text{Si}(|k_1 \tau_R|) \right)^2 \right]^2 \frac{k_1^2}{k_\star^2} \left(1 + \frac{k_1^2}{4k_\star^2} \right)^2 \left(1 + \frac{k_1^4}{16k_\star^4} \right) \\ &= \frac{2}{\pi^3} \bar{\mathcal{P}}_h^2(k_1) \frac{k_1^2}{k_\star^2} \left(1 + \frac{k_1^2}{4k_\star^2} \right)^{-2} \left(1 + \frac{k_1^4}{16k_\star^4} \right). \end{aligned} \quad (3.29)$$

under our hypothesis of sharply peaked magnetic spectrum. The amplitude of the contribution we computed for the GW trispectrum in the flattened shape is then proportional to the square of the GW power spectrum, times a simple polynomial function of the momentum scale. The other contributions to J_B from the aforementioned permutations, being associated to similar diagrams, are expected to give similar results. The presence of the δ -function magnetic spectrum leads to a dependence on k/k_\star which is analogous to the one observed for the two-point function case, where the signal grows and then exhibits a sharp cutoff for $k/k_\star = 2$. Therefore, the present discussion, although preliminary, already illustrates the mechanism by which the magnetic source shapes the GW trispectrum and the associated momentum dependence in this particular case.

Summary of this Section Let us summarize the results of this theoretical Section. We find that vector-induced GW backgrounds are characterized by intrinsic stationary non-Gaussianities. The connected part of the primordial trispectrum acquires an amplitude proportional to the square

of GW power spectrum, and a shape corresponding to a flattened quadrilateral shape with all sides superimposed: see Fig. 3, right panel.

The scaling of the connected trispectrum amplitude as \mathcal{P}_h^2 —rather than \mathcal{P}_h^3 , as would be expected for a standard “local-type” expansion of GW non-Gaussian mode functions—implies that its magnitude can be parametrically enhanced. The characteristic folded shape of the trispectrum motivates the notion of *stationary GW non-Gaussianity*, introduced in Section 3 as a mechanism to address the detectability challenges emphasized in [67, 68]. In the specific case of a delta-function magnetic power spectrum source, the momentum dependence of the trispectrum can be derived analytically, yielding a flattened quadrilateral configuration with equal sides. For more general sources, we expect a broader range of momentum dependences, while still preserving the underlying folded quadrilateral geometry. We now turn to the observational implications of these results and analyze their phenomenological consequences for gravitational-wave experiments.

4 Consequences for GW experiments

Motivations We now investigate implications for GW experiments of non-Gaussian correlators in the SGWB from the early universe, with the geometrical characteristics analysed in the previous Sections – i.e. a flattened shape for the trispectrum, whose momenta are aligned along a common direction \hat{n} and their size satisfies

$$k_1 + k_3 = k_2 + k_4 \quad (4.1)$$

The polarization indexes in circular basis are such that the four-point correlator preserves helicity, see Eq. (3.5). There are two complementary strategies to pursue to test GW non-Gaussianities:

- We may examine how a sizeable GW trispectrum in a flattened configuration *modulates* the statistical properties of the two-point function and of the gravitational-wave power spectrum, thereby inducing distinctive and potentially observable signatures.
- Alternatively, we can study the *direct detectability* of higher-order correlators, such as the GW four-point function, by analyzing the response of GW experiments to this observable, and assessing the corresponding detection prospects. Since the trispectrum amplitude scales as $\mathcal{T}_h \propto \mathcal{P}_h^2$, the detectability of this quantity depends on the values of the GW two-point correlator.

We consider examples of both approaches, respectively in Section 4.1 and 4.2. We begin by presenting a schematic and general discussion of the underlying physical effects we are going to investigate.

A typical GW signal s_A measured by a GW experiment labeled with A is given by the contraction of the GW $h_{ij}(\tau, \mathbf{x})$ with the so-called detector tensor d_A^{ij}

$$s_A = h_{ij} d_A^{ij}, \quad (4.2)$$

the latter quantity depends on the geometric configuration of the GW detector, and its properties. We assume the corresponding measurement to be made at time τ and at position \mathbf{x}_A ⁴. We define

⁴More realistically, as we will learn in the next subsections, the results depend on various locations as the Earth

the combination

$$d_A^{(\lambda)}(\hat{n}) = e_{ij}^{(\lambda)}(\hat{n}) d_A^{ij}, \quad (4.3)$$

with \hat{n} the GW direction. Computing the signal two-point function, and passing to Fourier space, we have

$$\begin{aligned} \langle s_A(\tau, \mathbf{x}_A) s_B(\tau, \mathbf{x}_B) \rangle &= \sum_{\lambda} \int k^2 dk \frac{d^2 \hat{n}}{(2\pi)^3} d_A^{(\lambda)}(\hat{n}) d_B^{(-\lambda)}(\hat{n}) e^{ik \hat{n} (\mathbf{x}_A - \mathbf{x}_B)} \langle h_{\mathbf{k}}^{(\lambda)} h_{\mathbf{k}}^{(-\lambda)} \rangle_{\Delta} \\ &= 2 \int d \ln k \gamma_{AB}(k) \mathcal{P}_h(k), \end{aligned} \quad (4.4)$$

where

$$\gamma_{AB} = \frac{1}{4\pi} \int d^2 \hat{n} \left(\sum_{\lambda} d_A^{(\lambda)}(\hat{n}) d_B^{(-\lambda)}(\hat{n}) \right) e^{ik \hat{n} (\mathbf{x}_A - \mathbf{x}_B)} \quad (4.5)$$

is the so-called *overlap reduction function* (ORF) which controls how the signal two-point correlations depend on the detector properties and configuration ⁵.

The ORF is the bridge between theoretical predictions of GW properties – as the GW power spectrum – and experimental quantities. Its features allow us to investigate whether the measured signal is due to a GW background. For example, data distributed following Hellings-Downs curve in pulsar timing array measurements (more on this in Section 4.1) offer circumstantial evidence for a GW interpretation of the measured GW signal.

The variance of the ORF. The ORF can be interpreted as arising from the *mean value* in an ensemble average of GW measurements. Hence its properties can be characterized by a *variance*, which should be taken into account when confronting theory with experiment [69]. There are several possible contributions to the variance of an ORF, depending on the experiment under consideration. Let us schematically estimate the contribution of connected four-point function to what was dubbed *total variance* ⁶ of the ORF in [70]. It is defined as

$$\sigma_{AB}^2 = \langle s_A s_B s_A s_B \rangle - \langle s_A s_B \rangle^2. \quad (4.6)$$

Besides its disconnected parts, let us assume a non-vanishing connected contribution to the trispectrum, characterized by a flattened shape as discussed in Section 3. This implies that all momenta are forced to align along a common direction \hat{n} . The connected part of the signal four-point function – associated with the connected trispectrum – can then be expressed as

$$\langle s_A s_B s_A s_B \rangle_{\text{conn}} = \frac{1}{4\pi^2} \int d \ln k_1 d \ln k_2 d \ln k_3 dk_4 \mathcal{T}_h(k_i) \Sigma_{\text{conn}}^2, \quad (4.7)$$

and pulsar positions in pulsar timing arrays or the vertexes of interferometer arms. We adopt this preliminary simplification to make our arguments more transparent.

⁵The overall factor controlling the ORF normalization in Eq. (4.5) can change depending on conventions for each type of GW experiment. We will be explicit on the normalization definitions in what comes next.

⁶Although [70] focuses on pulsar timing arrays, their definition of total variance can be in principle applied to more general GW experiments.

where (we use the specific trispectrum definition of (3.5))

$$\begin{aligned}
\Sigma_{\text{conn}}^2 &= \frac{1}{4\pi} \int d^2 n d^2 n_2 d^2 n_3 d^2 n_4 \delta(\hat{n} - \hat{n}_2) \delta(\hat{n} - \hat{n}_3) \delta(\hat{n} - \hat{n}_4) \delta(k_1 + k_3 - k_2 - k_4) \\
&\quad \times \left(\sum_{\lambda_{1,2}=\pm 2} d_A^{(\lambda_1)}(\hat{n}) d_B^{(-\lambda_1)}(\hat{n}) d_A^{(\lambda_2)}(\hat{n}) d_B^{(-\lambda_2)}(\hat{n}) \right) e^{ik_1 \hat{n} \cdot \mathbf{x}_A - ik_2 \hat{n}_2 \cdot \mathbf{x}_B + ik_3 \hat{n}_3 \cdot \mathbf{x}_A - ik_4 \hat{n}_4 \cdot \mathbf{x}_B} \\
&= \frac{1}{4\pi} \int d^2 \hat{n} \left(\sum_{\lambda_{1,2}=\pm 2} d_A^{(\lambda_1)}(\hat{n}) d_B^{(-\lambda_1)}(\hat{n}) d_A^{(\lambda_2)}(\hat{n}) d_B^{(-\lambda_2)}(\hat{n}) \right) e^{i(k_1+k_3) \hat{n} \cdot (\mathbf{x}_A - \mathbf{x}_B)}, \quad (4.8)
\end{aligned}$$

and we make use of the condition of alignment of all four momenta along a common direction \hat{n} , and the sum over polarization indexes satisfy the helicity conservation Eq (3.3).

Assembling the connected result in Eq.(4.7) with the disconnected contributions, we can easily compute the total variance as

$$\begin{aligned}
\sigma_{AB}^2 &= \langle s_{ASB} s_{ASB} \rangle - \langle s_{ASB} \rangle^2 \quad (4.9) \\
&= \int d \ln k_1 d \ln k_2 \mathcal{P}_h(k_1) \mathcal{P}_h(k_2) \left[\Sigma_{\text{disc}}^2(k_1, k_2) + \int d \ln k_3 \frac{\mathcal{T}_h(k_1, k_2, k_3)}{\mathcal{P}_h(k_1) \mathcal{P}_h(k_2)} \Sigma_{\text{conn}}^2(k_1, k_2) \right] \quad (4.10)
\end{aligned}$$

with

$$\Sigma_{\text{disc}}^2(k_1, k_2) = \gamma_{AB}(k_1) \gamma_{AB}(k_2) + \gamma_{AA}(k_1) \gamma_{AA}(k_2) \quad (4.11)$$

and Σ_{conn}^2 is given in Eq. (4.8). The first two terms within parenthesis of Eq. (4.10) depend on the disconnected contributions to the four-point function, while the last term depends on its connected part. Hence, Eq. (4.10) indicates that the connected GW trispectrum in a flattened configuration contributes to the total variance of the two-point function. Consequently, it potentially affects GW measurements. In the examples discussed in Section 3, the amplitude of the trispectrum is proportional to the square of the power spectrum amplitude, hence we can expect an order-one value for the integral over $d \ln k_3$, contributing to the last term within parenthesis of Eq. (4.10). The contribution to the variance of the connected trispectrum – in such set-up – should be comparable to the one of the disconnected parts of the four-point function. This fact is particularly relevant for pulsar timing arrays, see Section 4.1.

The ORF for the four-point function of GW signals. Besides a modulation of the GW two point function, as a matter of principle a connected trispectrum can be measured directly by taking the four-point function of the GW signal, and extracting its connected component exploiting its associated ORF. Assuming that the trispectrum shape acquires only a flattened configuration, within the hypothesis discussed above, we compute the associated four-point ORF

through the formula

$$\gamma_{ABCD} = \frac{1}{4\pi} \int d^2\hat{n} \left(\sum_{\lambda_{1,2}=\pm 2} d_A^{(\lambda_1)} d_B^{(-\lambda_1)} d_A^{(\lambda_2)} d_B^{(-\lambda_2)} \right) e^{ik_1 \hat{n} \cdot (\mathbf{x}_A - \mathbf{x}_D)} e^{-ik_2 \hat{n} \cdot (\mathbf{x}_B - \mathbf{x}_D)} e^{ik_3 \hat{n} \cdot (\mathbf{x}_C - \mathbf{x}_D)} \quad (4.12)$$

where all the d 's depend on the common GW direction \hat{n} and the x 's are the detector positions. The polarization indexes satisfy the helicity condition (3.3), and the momenta – aligned along \hat{n} – satisfy the condition (4.1). The previous angular integral leads to the four-point ORF and, as we shall see in Section 4.2, it can be performed analytically – at least in the case of ground-based detectors.

4.1 Pulsar timing arrays

Pulsar timing arrays (PTA) offer a powerful method for searching for the SGWB background at nano-Hertz frequencies, which recently lead to significant hints of detection [71–74]. Time delays on the pulsar periods, indicated with $z(t)$, or the corresponding time residuals called $R(t)$, are used as indicators of the presence of a SGWB. We refer to [65] for a pedagogical discussion of basic concepts and techniques in PTA physics. The recent preliminary measurements of the SGWB at nano-Hz frequencies might also be explained by certain models of second order, induced GW (see e.g. [75]), similar to the scenarios we consider in our work. Hence it is very relevant to study implications of GW non-Gaussianities in this context.

The ORF corresponding to the PTA time-delay two-point functions has been first computed by Hellings and Downs in [76]. The detector tensor d_A^{ij} of Eq. (4.2) reads in this context

$$d_A^{ij} = \frac{n^i n^j}{2(1 + \hat{x}_A \cdot \hat{n})} \quad (4.13)$$

where \hat{n} is the GW direction, and \hat{x}_A the direction of pulsar A with respect to the Earth position. The ORF leading to the Hellings-Downs curve correlate GW signals measured with two pulsars A and B . It is given by the integral in Eq. (4.5), sometimes multiplied by a conventional normalization factor $3/4$ – see e.g. [77]. As customary, we neglect the so-called *pulsar-term* contributions, which cancel upon integration unless two pulsars are coincident. Under this assumption, the resulting integral becomes independent of the specific pulsar locations, as well as on the GW frequency. It reads

$$\gamma_{AB}(\zeta) = \frac{3}{2} \frac{1 - \cos \zeta}{2} \ln \left(\frac{1 - \cos \zeta}{2} \right) - \frac{1}{4} \frac{1 - \cos \zeta}{2} + \frac{1}{2} (1 + \delta_{AB}). \quad (4.14)$$

where ζ is the angle between the vectors pointing from the Earth towards pulsar A and B respectively. In the limit of coincident pulsars, $A = B$, the pulsar term becomes important leading to the Kronecker function δ_{AB} in Eq.(4.14). See e.g. [78].

The Hellings-Downs curve is a central quantity in PTA measurements – its characteristics angular correlations is a crucial test for determining the GW origin of PTA measurements. Recently, much work has been devoted in computing and physically characterizing the *variance* of

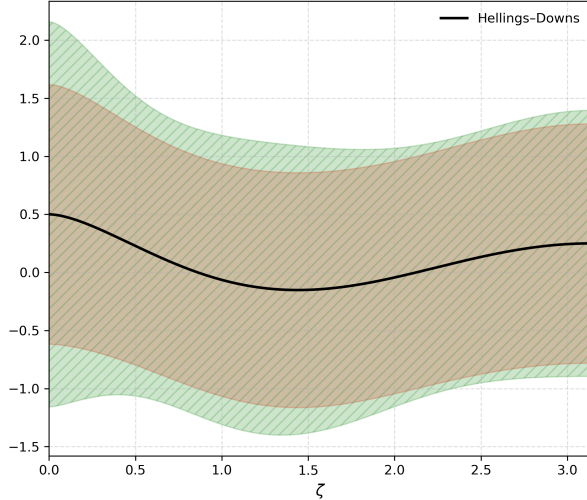


Figure 5: Representation of the Hellings-Downs function (black line); its total variance associated with disconnected contributions to the signal four-point function (brown band); finally, the total variance accounting for non-vanishing contributions of the connected GW trispectrum (green band). See main text for details.

Hellings-Downs correlators [69, 70, 78–88]. There are several different contributions to the variance of this curve. Following the arguments of Section 3, we are interested to the so-called total variance (dubbed in this way in [70]). The total variance corresponds to the expected uncertainty for a *single pulsar pair* whose time delays are caused and correlated by the gravitational-wave background. It is associated with the four-point function of Eq. (4.19). It is constituted by two pieces, a disconnected part – already discussed in the literature – and a connected one – which we include here for the first time. The disconnected part is the total variance studied in [70],

$$\Sigma_{\text{disc}}^2 = \gamma_{AB}^2 + \gamma_{AA}^2 \quad (4.15)$$

which is easily computable from Eq.(4.14). It coincides with the results of [70].

We compute for the first time the connected part contribution – last term of Eq. (4.10) and in particular the quantity in Eq (4.8), including an overall factor of 3/4 to match with the aforementioned Hellings-Downs normalization convention. See also [59] for another example of possible contribution of GW four-point functions to Hellings-Downs–type correlations. Recall that we need to sum over all polarizations satisfying Eq. (3.4), and we specialize to our definition of trispectrum of Eq.(3.5). We find

$$\Sigma_{\text{conn}}^2 = \frac{3}{16\pi} \int d^2n \left[\left(\sum_{\lambda_i} d_A^{(\lambda_1)}(\hat{n}) d_B^{(-\lambda_1)}(\hat{n}) d_A^{(\lambda_2)}(\hat{n}) d_B^{(-\lambda_2)}(\hat{n}) \right) \right] \quad (4.16)$$

$$= \frac{1}{40} [6 + (134 - 139y)y + 30y(2 + 3y) \ln y] , \quad (4.17)$$

where we call $y = (1 - \cos \zeta)/2$, and we denote $(d_A^{(L)} d_B^{(R)}) = d_A^{ij} d_B^{pq} e_{ij}^{(L)} e_{pq}^{(R)}$. We plot in Fig. 5

the Hellings-Downs ORF $\gamma_{AB}(\zeta)$ as a function of the angle among pulsars. We include the effect of variances in color bands. In red band, the disconnected contribution to the variance, delimited within the region $\gamma_{AB} \pm \Sigma_{\text{disc}}$. (Compare with Fig 1 of [70]). In green band, the new connected contribution, within the region $\gamma_{AB} \pm \sqrt{\Sigma_{\text{disc}}^2 + 10 \Sigma_{\text{conn}}^2}$. (We set to 10 the integral over $\ln k_3$ in Eq. (4.10), in order to make more clear the angular dependence of the result.) We learn that the connected part of the GW non-Gaussianity can increase the total variance of the Hellings-Downs ORF, hence allowing for scattering of experimental data around the mean Hellings-Downs ORF for single pulsar-pair measurements. It would be interesting in the future to further study the observational implications on PTA data of the amplification effects on the size of the variance induced by the connected part of the non-Gaussian GW trispectrum.

4.2 Ground-based detectors

We now outline the analytical computation of the ORF four-point function defined in Eq. (4.12), which is the key observable for directly probing the connected component of the signal four-point correlator. Improvements in the sensitivity of ground-based detector networks, both within the LVK array [89–91] and in future facilities such as the Einstein Telescope [92], open new opportunities to detect primordial SGWBs in the frequency range of tens of Hertz, should such signals exist. Cosmological sources capable of producing backgrounds in this band, including second-order induced SGWBs, are reviewed in [93]. It is therefore essential to investigate their detectability prospects in scenarios where the signal is non-Gaussian, as in the framework considered here. Although we do not present explicit detection forecasts—since these depend on the detailed frequency dependence of the four-point correlators—we emphasize that, because the trispectrum amplitude scales as \mathcal{P}_h^2 , it can be significantly enhanced in frequency intervals where the gravitational-wave signal itself is amplified, as in the second order GW induced scenarios explored in previous sections. In our analysis of implications of GW non-Gaussianities, an advantage of ground-based detectors is that the relevant integrals as Eq.(4.12) can be evaluated analytically. For example, the ORF for correlations among two detectors is well-known, see e.g. [93]. Here we consider correlating measurements of a non-Gaussian stochastic gravitational-wave background (SGWB) across *four* distinct detectors—explicit examples to have in mind being LIGO Hanford, LIGO Livingston, Virgo, and KAGRA. In the presence of a connected gravitational-wave trispectrum, such a four-detector correlation is non-vanishing and, in principle, observable.

Assuming equal-length detector arms, the detector tensor d_A^{ij} reads in this case

$$d_A^{ab} = \frac{1}{2} \left(u_A^a u_A^b - v_A^a v_A^b \right) \quad (4.18)$$

with $\mathbf{u}_A, \mathbf{v}_A$ denoting the directions in three-dimensional space of the arms of the interferometer denoted with the index A . Notice the tracelessness condition $d_A^{ii} = 0$, as well as the fact that d_A^{ij} is now independent from the GW direction \hat{n} and momentum. In this set-up, we can write

Eq. (4.12) as follows

$$\gamma_{ABCD}(k_1, k_2) = \frac{d_A^{ab} d_B^{cd} d_C^{ef} d_D^{gh}}{4\pi} \int d^2 \hat{n} \Lambda_{abcd}(\hat{n}) \Lambda_{efgh}(\hat{n}) e^{ik_1 \hat{n} \cdot (\mathbf{x}_A - \mathbf{x}_D)} e^{-ik_2 \hat{n} \cdot (\mathbf{x}_B - \mathbf{x}_D)} e^{ik_3 \hat{n} \cdot (\mathbf{x}_C - \mathbf{x}_D)}, \quad (4.19)$$

where we use identity (2.11), we impose the helicity condition (3.4) and condition (3.2) on GW momenta direction, as well as the flattened shape condition for the trispectrum along a GW direction \hat{n} (see Fig. 3, right panel).

To proceed, generalizing [93] to the case of connected four point functions, we introduce the combinations

$$\alpha = k_1 |\mathbf{x}_A - \mathbf{x}_D| - k_2 |\mathbf{x}_B - \mathbf{x}_D| + k_3 |\mathbf{x}_C - \mathbf{x}_D| \quad (4.20)$$

$$\hat{s} = \frac{k_1 (\mathbf{x}_A - \mathbf{x}_D) - k_2 (\mathbf{x}_B - \mathbf{x}_D) + k_3 (\mathbf{x}_C - \mathbf{x}_D)}{k_1 |\mathbf{x}_A - \mathbf{x}_D| - k_2 |\mathbf{x}_B - \mathbf{x}_D| + k_3 |\mathbf{x}_C - \mathbf{x}_D|}, \quad (4.21)$$

which corresponds to a weighted size α of GW momenta, and an average direction \hat{s} . We recall the relation Eq. (2.11), between the projector tensor Λ and the GW direction \hat{n} : once expanded over its contributions it reads

$$\begin{aligned} 2\Lambda_{abcd} &= \delta_{ad}\delta_{bc} + \delta_{ac}\delta_{bd} - \delta_{ab}\delta_{cd} \\ &+ \delta_{cd}\hat{n}_a\hat{n}_b + \delta_{ab}\hat{n}_c\hat{n}_d - \delta_{bd}\hat{n}_a\hat{n}_c - \delta_{ac}\hat{n}_b\hat{n}_d - \delta_{bc}\hat{n}_a\hat{n}_d - \delta_{ad}\hat{n}_b\hat{n}_c \\ &+ \hat{n}_a\hat{n}_b\hat{n}_c\hat{n}_d. \end{aligned} \quad (4.22)$$

It is then convenient to define the following combinations controlling correlations among two detectors

$$F_{AB}^{(0)} = \frac{1}{2} d_A^{ab} d_B^{cd} (\delta_{ac}\delta_{bd} + \text{perms}), \quad (4.23)$$

$$F_{AB}^{(2)} = -\frac{1}{2} d_A^{ab} d_B^{cd} (\delta_{ac}n_b n_d + \text{perms}), \quad (4.24)$$

$$F_{AB}^{(4)} = \frac{1}{2} d_A^{ab} d_B^{cd} n_a n_b n_c n_d, \quad (4.25)$$

where the index (p) indicates the power of unit vector \hat{n} involved. The integral to deal with formally becomes

$$\gamma_{ABCD} = \frac{1}{4\pi} \int d^2 \hat{n} \left(F_{AB}^{(0)} + F_{AB}^{(2)} + F_{AB}^{(4)} \right) \left(F_{CD}^{(0)} + F_{CD}^{(2)} + F_{CD}^{(4)} \right) e^{i\alpha \hat{s} \cdot \hat{n}}. \quad (4.26)$$

We multiply the two parenthesis in Eq. (4.26), and define the following combinations

$$G_{ABCD}^{(0)} = F_{AB}^{(0)} F_{CD}^{(0)}, \quad (4.27)$$

$$G_{ABCD}^{(2)} = F_{AB}^{(2)} F_{CD}^{(0)} + F_{AB}^{(0)} F_{CD}^{(2)}, \quad (4.28)$$

$$\dots = \dots \quad (4.29)$$

$$G_{ABCD}^{(8)} = F_{AB}^{(4)} F_{CD}^{(4)}, \quad (4.30)$$

which depend on all four detectors, and assemble the powers of unit vector \hat{n} . We can now use the identity

$$e^{i\alpha\hat{n}\cdot\hat{s}} = \sum_{\ell=0}^{\infty} i^{\ell} (2\ell+1) j_{\ell}(\alpha) P_{\ell}(\hat{n}\cdot\hat{s}), \quad (4.31)$$

with j_{ℓ} the spherical Bessel function, and P_{ℓ} the Legendre polynomial of order ℓ . Plugging into Eq. (4.26) and expanding, we find that ORF can be expressed as

$$\gamma_{ABCD} = \sum_{n=0}^4 I^{(2n)} \quad (4.32)$$

where each $I^{(2n)}$ reads

$$I^{(2n)} = \sum_{\ell=0}^n (-)^{\ell} \frac{(4\ell+1)}{4\pi} j_{2\ell}(\alpha) \int d^2n P_{2\ell}(\hat{n}\cdot\hat{s}) G^{(2n)}(\hat{n}). \quad (4.33)$$

Hence we reduce the problem to compute integrals of Legendre polynomials, weighted by polynomials in \hat{n} – a straightforward operation which can be carried on analytically.

For example, let us work out explicitly the computation for $I^{(0)}$

$$I^{(0)} = \frac{j_0(\alpha)}{4\pi} \int d^2n P_0(\hat{n}\cdot\hat{s}) G^{(0)}(\hat{n}) \quad (4.34)$$

$$= \frac{j_0(\alpha)}{4\pi} \left(d_A^{ab} d_B^{ab} \right) \left(d_C^{cd} d_D^{cd} \right) \int d^2n P_0(\hat{n}\cdot\hat{s}) \quad (4.35)$$

$$= \frac{\sin \alpha}{\alpha} \text{tr}(d_{AB}) \text{tr}(d_{CD}), \quad (4.36)$$

where we use the abbreviation $\text{tr}(d_{AB}) = (d_A^{ab} d_B^{ab})$.

The other four contributions $I^{(2)}$, $I^{(4)}$, $I^{(6)}$, $I^{(8)}$ can be computed analogously. For example, using the abbreviation $(sd_{ABs}) = s_a s_c d_A^{ab} d_B^{bc}$, the expression for $I^{(2)}$ reads

$$I^{(2)} = -\frac{4j_1(\alpha)}{\alpha} \text{tr}(d_{AB}) \text{tr}(d_{CD}) + 2j_2(\alpha) (sd_{ABs}) \text{tr}(d_{CD}) + 2j_2(\alpha) (sd_{CDs}) \text{tr}(d_{AB}). \quad (4.37)$$

4.3 An optimal estimator

We now develop an estimator designed to optimally extract the connected part of the GW four-point correlation function. Our strategy follows the general philosophy of [93], suitably modified to the higher-correlator case. Throughout this section we keep the discussion as general as possible, without specifying a particular GW experiment.

Let the measured time-domain output of detector a be

$$\Sigma(t) = s(t) + n(t), \quad (4.38)$$

where $s(t)$ denotes the physical GW signal and $n(t)$ represents detector noise. We consider correlations among four such data streams $\Sigma(t)$ coming from independent detectors. The instrumental

noise is assumed to be stationary, Gaussian, and uncorrelated between different detectors. We work in the regime where the noise amplitude dominates over the signal, so that the variance of the estimator is governed by noise, while its expectation value is sourced entirely by the signal component $s(t)$. The GW signal measured by different detectors may exhibit non-Gaussian correlations, encoded in a non-vanishing four-point function $\langle s^4 \rangle$, which we assume to be stationary as discussed in Section 3.

To probe such correlations we construct an estimator built from three copies of the detector output. For a specific detector quartet (a, b, c, d) we define

$$S_{abcd} = \int_{-T/2}^{T/2} dt_1 \int_{-T/2}^{T/2} dt_2 \int_{-T/2}^{T/2} dt_3 \int_{-T/2}^{T/2} dt_4 \Sigma_a(t_1) \Sigma_b(t_2) \Sigma_c(t_3) \Sigma_c(t_4) Q(t_2 - t_1, t_3 - t_1, t_4 - t_1), \quad (4.39)$$

where T denotes the total observation time. The function Q acts as a filter kernel and depends only on time differences, consistent with the stationarity assumption. It is taken to vanish for sufficiently large separations $|t_i - t_j|$. Our goal will be to determine the form of Q that maximizes the response to the signal.

For the moment we focus on a single detector quartet (a, b, c, d) . The time series can be expressed in the frequency domain through

$$\Sigma(t) = \int_{-\infty}^{\infty} df e^{2\pi i f t} \tilde{\Sigma}(f). \quad (4.40)$$

Notice that frequencies run also along negative values. Substituting this representation into Eq. (4.39) gives

$$S_{abcd} = \int_{-\infty}^{\infty} df_1 df_2 df_3 df_4 \delta_T(f_1 + f_2 + f_3 + f_4) \tilde{\Sigma}_a(f_1) \tilde{\Sigma}_b(f_2) \tilde{\Sigma}_c(f_3) \tilde{\Sigma}_d(f_4) \tilde{Q}^*(f_2, f_3, f_4), \quad (4.41)$$

where the finite-time delta function is defined as

$$\delta_T(f) \equiv \int_{-T/2}^{T/2} dt e^{2\pi i f t}, \quad \delta_T(0) = T. \quad (4.42)$$

In the noise-dominated limit the expectation value and variance of the statistic read

$$\mu = \langle S_{abcd} \rangle, \quad (4.43)$$

$$\sigma^2 = \langle S_{abcd}^2 \rangle - \mu^2. \quad (4.44)$$

Because the detector noise is Gaussian, the mean μ receives contributions only from the GW signal, whereas the variance is determined by the noise. Since the signal is assumed much smaller than the noise, the μ^2 term in Eq. (4.44) can be neglected. The signal-to-noise ratio (SNR) of the estimator is therefore

$$\text{SNR} = \frac{\mu}{\sigma}, \quad (4.45)$$

and the optimization problem reduces to finding the filter Q that maximizes this quantity.

A straightforward calculation yields

$$\mu = T \kappa_{abcd} \int_{-\infty}^{\infty} df_1 df_2 df_3 \mathcal{T}_h(f_1, f_2, f_3) \tilde{Q}^*(f_1, f_2, f_3), \quad (4.46)$$

where κ_{abcd} denotes the four-detector overlap reduction function and \mathcal{T}_h is the connected contribution to the GW trispectrum. The frequencies satisfy the condition $f_1 + f_2 + f_3 + f_4 = 0$.

Let $\sigma_a^2(f)$ denote the noise power spectral density for detector a . The noise correlator is then

$$\langle n_a(f_1) n_b(f_2) \rangle = \delta(f_1 + f_2) \delta_{ab} \sigma_a^2(f_1). \quad (4.47)$$

Assuming Gaussian noise, the variance of the estimator becomes

$$\sigma^2 = T \int_{-\infty}^{\infty} df_1 df_2 df_3 N_{abcd}(f_1, f_2, f_3) |Q(f_1, f_2, f_3)|^2, \quad (4.48)$$

with

$$N_{abc}(f_1, f_2, f_3) = \sigma_a^2(f_1) \sigma_b^2(f_2) \sigma_c^2(f_3) \sigma_d^2(f_1 + f_2 + f_3) + \text{perms.} \quad (4.49)$$

The resulting SNR can therefore be written as

$$\text{SNR} = \sqrt{T} \frac{\kappa_{abcd} \int df_1 df_2 df_3 \mathcal{T}_h(f_1, f_2, f_3) \tilde{Q}^*(f_1, f_2, f_3)}{[\int df_1 df_2 df_3 N_{abcd}(f_1, f_2, f_3) |Q(f_1, f_2, f_3)|^2]^{1/2}}. \quad (4.50)$$

To determine the optimal filter we employ the Wiener filtering method (see e.g. [93]). We introduce the inner product

$$(C, D) \equiv \int df_1 df_2 df_3 C(f_1, f_2, f_3) D^*(f_1, f_2, f_3) N_{abcd}(f_1, f_2, f_3), \quad (4.51)$$

which allows us to rewrite the SNR as

$$\text{SNR} = \sqrt{T} \frac{(\kappa_{abcd} \mathcal{T}_h / N_{abcd}, Q)}{[(Q, Q)]^{1/2}}. \quad (4.52)$$

Maximization with respect to Q leads to the optimal choice

$$Q(f_1, f_2, f_3) = \frac{\kappa_{abcd} \mathcal{T}_h(f_1, f_2, f_3)}{N_{abcd}(f_1, f_2, f_3)}. \quad (4.53)$$

Substituting this expression back into the SNR yields the maximal achievable value

$$\text{SNR}_{\text{max}} = \sqrt{T} \left[\int df_1 df_2 df_3 \frac{(\kappa_{abcd} \mathcal{T}_h(f_1, f_2, f_3))^2}{N_{abcd}(f_1, f_2, f_3)} \right]^{1/2}. \quad (4.54)$$

Further simplification arises when the noise spectrum is approximately frequency independent,

$$\langle n_a(f_1) n_b(f_2) \rangle = \delta(f_1 + f_2) \delta_{ab} \sigma_a^2, \quad (4.55)$$

which implies

$$N_{abcd} = 4 \sigma_a^2 \sigma_b^2 \sigma_c^2 \sigma_d^2. \quad (4.56)$$

In this case the maximal signal-to-noise ratio becomes

$$\text{SNR}_{\max} = \sqrt{\frac{T}{4}} \left[\int df_1 df_2 df_3 \frac{(\kappa_{abcd} \mathcal{T}_h(f_1, f_2, f_3))^2}{\sigma_a^2 \sigma_b^2 \sigma_c^2 \sigma_d^2} \right]^{1/2}. \quad (4.57)$$

The result above applies to a single detector quadruplet. In experiments where multiple independent quadruplets can be formed, such as pulsar timing arrays, the total signal-to-noise ratio can be enhanced by summing the contributions from all available combinations.

Acknowledgments

It is a pleasure to thank Jinn-Ouk Gong, Maria Mylova, and Misao Sasaki for discussions on related subjects. GT is partially funded by the STFC grants ST/T000813/1 and ST/X000648/1.

A The time integral of Eq. (3.7)

We present here the derivation of the late-time limit result of the integral in eq. (3.7) in radiation dominated era.

The integral to compute is

$$J_\tau(\tau) = \prod_{i=1}^4 \int d\tau_i \frac{g_{k_i}(\tau, \tau_i)}{a(\tau_i)} \quad (A.1)$$

where

$$g_{k_i}(\tau, \tau_i) = \frac{i}{2k_i} \left(e^{-ik_i(\tau-\tau_i)} - e^{ik_i(\tau-\tau_i)} \right). \quad (A.2)$$

The result of the full integral is

$$\begin{aligned} J_\tau(\tau) = & \frac{1}{16k_1 k_2 k_3 k_4} \left[-\text{Ci}(k_1 \tau_R) \sin(k_1 \tau) + \text{Ci}(k_1 \tau) \sin(k_1 \tau) + \cos(k_1 \tau) (\text{Si}(k_1 \tau_R) - \text{Si}(k_1 \tau)) \right] \\ & \times \left[-\text{Ci}(k_2 \tau_R) \sin(k_2 \tau) + \text{Ci}(k_2 \tau) \sin(k_2 \tau) + \cos(k_2 \tau) (\text{Si}(k_2 \tau_R) - \text{Si}(k_2 \tau)) \right] \\ & \times \left[-\text{Ci}(k_3 \tau_R) \sin(k_3 \tau) + \text{Ci}(k_3 \tau) \sin(k_3 \tau) + \cos(k_3 \tau) (\text{Si}(k_3 \tau_R) - \text{Si}(k_3 \tau)) \right] \\ & \times \left[-\text{Ci}(k_4 \tau_R) \sin(k_4 \tau) + \text{Ci}(k_4 \tau) \sin(k_4 \tau) + \cos(k_4 \tau) (\text{Si}(k_4 \tau_R) - \text{Si}(k_4 \tau)) \right]. \end{aligned} \quad (A.3)$$

Using the asymptotic behaviour $\text{Ci}(k\tau) \xrightarrow{\tau \rightarrow \infty} 0$, $\text{Si}(k\tau) \xrightarrow{\tau \rightarrow \infty} \frac{\pi}{2}$, expanding the cos and sin functions in exponential form and renaming $\mathcal{C}(k_i) = (16k_1k_2k_3k_4)^{-1}$ we find

$$\begin{aligned}
J_\tau(\tau) &= \frac{C(k_i)}{16} [\pi^4 e^{-i(k_1+k_2+k_3+k_4)\tau} + \pi^4 e^{2ik_1\tau - i(k_1+k_2+k_3+k_4)\tau} + \pi^4 e^{2ik_2\tau - i(k_1+k_2+k_3+k_4)\tau} \\
&+ \cdots (1938) \cdots] + \\
&+ e^{2ik_1\tau + 2ik_3\tau + 2ik_4\tau - i(k_1+k_2+k_3+k_4)\tau} \text{Si}[k_1\tau_R] \text{Si}[k_2\tau_R] \text{Si}[k_3\tau_R] \text{Si}[k_4\tau_R] \\
&+ e^{2ik_2\tau + 2ik_3\tau + 2ik_4\tau - i(k_1+k_2+k_3+k_4)\tau} \text{Si}[k_1\tau_R] \text{Si}[k_2\tau_R] \text{Si}[k_3\tau_R] \text{Si}[k_4\tau_R] \\
&+ e^{2ik_1\tau + 2ik_2\tau + 2ik_4\tau - i(k_1+k_2+k_3+k_4)\tau} \text{Si}[k_1\tau_R] \text{Si}[k_2\tau_R] \text{Si}[k_3\tau_R] \text{Si}[k_4\tau_R] \\
&+ e^{2ik_1\tau + 2ik_2\tau + 2ik_3\tau - i(k_1+k_2+k_3+k_4)\tau} \text{Si}[k_1\tau_R] \text{Si}[k_2\tau_R] \text{Si}[k_3\tau_R] \text{Si}[k_4\tau_R].
\end{aligned} \tag{A.4}$$

Without conditions, taking the average over rapid oscillations leads to a vanishing result. By imposing that $s_i = +1$ for all i , and $k_4 = k_1 + k_3 - k_2$, we get

$$\begin{aligned}
J_\tau(\tau) &= C(k_i) \left\{ \text{Ci}(k_3\tau_R) \left[\frac{\text{Ci}(k_2\tau_R)}{2\pi} (\pi - 2\text{Si}(k_1\tau_R)) - \frac{\text{Ci}(k_1\tau_R)}{2\pi} (\pi - 2\text{Si}(k_2\tau_R)) \right] \right. \\
&+ \frac{1}{8\pi^2} (\pi - 2\text{Si}(k_1\tau_R)) (\pi - 2\text{Si}(k_2\tau_R)) \\
&- \frac{1}{4\pi} (\pi - 2\text{Si}(k_1\tau_R)) (\pi - 2\text{Si}(k_2\tau_R)) \text{Si}(k_3\tau_R) \\
&+ \text{Ci}(k_1\tau_R) \text{Ci}(k_2\tau_R) \left(\frac{\pi^2}{2} - \pi \text{Si}(k_3\tau_R) \right) + \text{Ci}((k_1 - k_2 + k_3)\tau_R) \\
&\times \left\{ \text{Ci}(k_3\tau_R) \left[2\text{Ci}(k_1\tau_R) \text{Ci}(k_2\tau_R) + \frac{1}{2} (\pi - 2\text{Si}(k_1\tau_R)) (\pi - 2\text{Si}(k_2\tau_R)) \right] \right. \\
&+ \text{Ci}(k_2\tau_R) (\pi - 2\text{Si}(k_1\tau_R)) \left(-\frac{\pi}{2} + \text{Si}(k_3\tau_R) \right) \\
&+ \left. \left. \text{Ci}(k_1\tau_R) \left[\frac{1}{2\pi} (\pi - 2\text{Si}(k_2\tau_R)) + (-\pi + 2\text{Si}(k_2\tau_R)) \text{Si}(k_3\tau_R) \right] \right\} \right. \\
&+ \left\{ \text{Ci}(k_3\tau_R) \left[\text{Ci}(k_2\tau_R) (-\pi + 2\text{Si}(k_1\tau_R)) + \text{Ci}(k_1\tau_R) (\pi - 2\text{Si}(k_2\tau_R)) \right] \right. \\
&- \frac{1}{4\pi} (\pi - 2\text{Si}(k_1\tau_R)) (\pi - 2\text{Si}(k_2\tau_R)) \\
&+ \frac{1}{2} (\pi - 2\text{Si}(k_1\tau_R)) (\pi - 2\text{Si}(k_2\tau_R)) \text{Si}(k_3\tau_R) \\
&+ \left. \left. \text{Ci}(k_1\tau_R) \text{Ci}(k_2\tau_R) (-\pi + 2\text{Si}(k_3\tau_R)) \right\} \text{Si}((k_1 - k_2 + k_3)\tau_R) \right\}.
\end{aligned}$$

By also imposing $k_2 = k_1$ and $k_3 = k_1$, corresponding to the configuration in the right panel of fig. 3, we get our familiar result of eq. (3.14)

$$\frac{1}{8k_1^4 H_0^4 \Omega_{\text{RD}}^2} \left[\text{Ci}(k_1 \tau_R)^2 + \left(\frac{\pi}{2} - \text{Si}(k_1 \tau_R) \right)^2 \right]^2 \quad (\text{A.5})$$

where we have restored the $H_0^4 \Omega_{\text{RD}}^2$ at denominator, since in the computation we have simply used $a(\tau) = \tau$.

References

- [1] C. Caprini and D. G. Figueroa, “Cosmological Backgrounds of Gravitational Waves,” *Class. Quant. Grav.* **35** no. 16, (2018) 163001, [arXiv:1801.04268](#) [[astro-ph.CO](#)].
- [2] O. Özsoy and G. Tasinato, “Inflation and Primordial Black Holes,” *Universe* **9** no. 5, (2023) 203, [arXiv:2301.03600](#) [[astro-ph.CO](#)].
- [3] R. Durrer and A. Neronov, “Cosmological Magnetic Fields: Their Generation, Evolution and Observation,” *Astron. Astrophys. Rev.* **21** (2013) 62, [arXiv:1303.7121](#) [[astro-ph.CO](#)].
- [4] M. Fabbrichesi, E. Gabrielli, and G. Lanfranchi, “The Dark Photon,” [arXiv:2005.01515](#) [[hep-ph](#)].
- [5] G. Domènech, “Scalar Induced Gravitational Waves Review,” *Universe* **7** no. 11, (2021) 398, [arXiv:2109.01398](#) [[gr-qc](#)].
- [6] **LISA Cosmology Working Group** Collaboration, J. E. Gammal *et al.*, “Reconstructing primordial curvature perturbations via scalar-induced gravitational waves with LISA,” *JCAP* **05** (2025) 062, [arXiv:2501.11320](#) [[astro-ph.CO](#)].
- [7] T. Regimbau, “The astrophysical gravitational wave stochastic background,” *Res. Astron. Astrophys.* **11** (2011) 369–390, [arXiv:1101.2762](#) [[astro-ph.CO](#)].
- [8] S. Kuroyanagi, T. Chiba, and T. Takahashi, “Probing the Universe through the Stochastic Gravitational Wave Background,” *JCAP* **11** (2018) 038, [arXiv:1807.00786](#) [[astro-ph.CO](#)].
- [9] C. Caprini, D. G. Figueroa, R. Flauger, G. Nardini, M. Peloso, M. Pieroni, A. Ricciardone, and G. Tasinato, “Reconstructing the spectral shape of a stochastic gravitational wave background with LISA,” *JCAP* **11** (2019) 017, [arXiv:1906.09244](#) [[astro-ph.CO](#)].
- [10] **LISA Cosmology Working Group** Collaboration, P. Auclair *et al.*, “Cosmology with the Laser Interferometer Space Antenna,” *Living Rev. Rel.* **26** no. 1, (2023) 5, [arXiv:2204.05434](#) [[astro-ph.CO](#)].
- [11] C. R. Contaldi, “Anisotropies of Gravitational Wave Backgrounds: A Line Of Sight Approach,” *Phys. Lett. B* **771** (2017) 9–12, [arXiv:1609.08168](#) [[astro-ph.CO](#)].
- [12] N. Bartolo, D. Bertacca, S. Matarrese, M. Peloso, A. Ricciardone, A. Riotto, and G. Tasinato, “Anisotropies and non-Gaussianity of the Cosmological Gravitational Wave Background,” *Phys. Rev. D* **100** no. 12, (2019) 121501, [arXiv:1908.00527](#) [[astro-ph.CO](#)].
- [13] N. Bartolo, D. Bertacca, S. Matarrese, M. Peloso, A. Ricciardone, A. Riotto, and G. Tasinato, “Characterizing the cosmological gravitational wave background: Anisotropies and non-Gaussianity,” *Phys. Rev. D* **102** no. 2, (2020) 023527, [arXiv:1912.09433](#) [[astro-ph.CO](#)].

- [14] **LISA Cosmology Working Group** Collaboration, N. Bartolo *et al.*, “Probing anisotropies of the Stochastic Gravitational Wave Background with LISA,” *JCAP* **11** (2022) 009, [arXiv:2201.08782 \[astro-ph.CO\]](#).
- [15] N. Bartolo, E. Komatsu, S. Matarrese, and A. Riotto, “Non-Gaussianity from inflation: Theory and observations,” *Phys. Rept.* **402** (2004) 103–266, [arXiv:astro-ph/0406398](#).
- [16] **Planck** Collaboration, P. A. R. Ade *et al.*, “Planck 2013 Results. XXIV. Constraints on primordial non-Gaussianity,” *Astron. Astrophys.* **571** (2014) A24, [arXiv:1303.5084 \[astro-ph.CO\]](#).
- [17] **Planck** Collaboration, Y. Akrami *et al.*, “Planck 2018 results. IX. Constraints on primordial non-Gaussianity,” *Astron. Astrophys.* **641** (2020) A9, [arXiv:1905.05697 \[astro-ph.CO\]](#).
- [18] B. Allen, “The Stochastic gravity wave background: Sources and detection,” in *Les Houches School of Physics: Astrophysical Sources of Gravitational Radiation*, pp. 373–417. 4, 1996. [arXiv:gr-qc/9604033](#).
- [19] P. Adshead and E. A. Lim, “3-pt Statistics of Cosmological Stochastic Gravitational Waves,” *Phys. Rev. D* **82** (2010) 024023, [arXiv:0912.1615 \[astro-ph.CO\]](#).
- [20] S. Drasco and E. E. Flanagan, “Detection methods for nonGaussian gravitational wave stochastic backgrounds,” *Phys. Rev. D* **67** (2003) 082003, [arXiv:gr-qc/0210032](#).
- [21] B. Allen, J. D. E. Creighton, E. E. Flanagan, and J. D. Romano, “Robust statistics for deterministic and stochastic gravitational waves in nonGaussian noise. 2. Bayesian analyses,” *Phys. Rev. D* **67** (2003) 122002, [arXiv:gr-qc/0205015](#).
- [22] N. Seto, “Non-Gaussianity test for discriminating gravitational wave backgrounds around 0.1-1Hz,” *Astrophys. J. Lett.* **683** (2008) L95–L98, [arXiv:0807.1151 \[astro-ph\]](#).
- [23] N. Seto, “Non-Gaussianity analysis of GW background made by short-duration burst signals,” *Phys. Rev. D* **80** (2009) 043003, [arXiv:0908.0228 \[gr-qc\]](#).
- [24] X.-J. Zhu, E. Howell, T. Regimbau, D. Blair, and Z.-H. Zhu, “Stochastic Gravitational Wave Background from Coalescing Binary Black Holes,” *Astrophys. J.* **739** (2011) 86, [arXiv:1104.3565 \[gr-qc\]](#).
- [25] L. Martellini and T. Regimbau, “Semiparametric approach to the detection of non-Gaussian gravitational wave stochastic backgrounds,” *Phys. Rev. D* **89** no. 12, (2014) 124009, [arXiv:1405.5775 \[astro-ph.CO\]](#).
- [26] N. J. Cornish and J. D. Romano, “When is a gravitational-wave signal stochastic?,” *Phys. Rev. D* **92** no. 4, (2015) 042001, [arXiv:1505.08084 \[gr-qc\]](#).
- [27] R. Buscicchio, A. Ain, M. Ballelli, G. Cella, and B. Patricelli, “Detecting non-Gaussian gravitational wave backgrounds: A unified framework,” *Phys. Rev. D* **107** no. 6, (2023) 063027, [arXiv:2209.01400 \[gr-qc\]](#).
- [28] M. Ballelli, R. Buscicchio, B. Patricelli, A. Ain, and G. Cella, “Improved detection statistics for non-Gaussian gravitational wave stochastic backgrounds,” *Phys. Rev. D* **107** no. 12, (2023) 124044, [arXiv:2212.10038 \[gr-qc\]](#).
- [29] J. Lawrence, K. Turbang, A. Matas, A. I. Renzini, N. van Remortel, and J. D. Romano, “A stochastic search for intermittent gravitational-wave backgrounds,” *Phys. Rev. D* **107** no. 10, (2023) 103026, [arXiv:2301.07675 \[gr-qc\]](#).
- [30] M. Falxa and A. Sesana, “Modeling Non-Gaussianities in Pulsar Timing Array data analysis using Gaussian Mixture Models,” [arXiv:2508.08365 \[astro-ph.IM\]](#).

- [31] J. D. Romano and N. J. Cornish, “Detection methods for stochastic gravitational-wave backgrounds: a unified treatment,” *Living Rev. Rel.* **20** no. 1, (2017) 2, [arXiv:1608.06889 \[gr-qc\]](#).
- [32] A. I. Renzini, B. Goncharov, A. C. Jenkins, and P. M. Meyers, “Stochastic Gravitational-Wave Backgrounds: Current Detection Efforts and Future Prospects,” *Galaxies* **10** no. 1, (2022) 34, [arXiv:2202.00178 \[gr-qc\]](#).
- [33] J. M. Maldacena and G. L. Pimentel, “On graviton non-Gaussianities during inflation,” *JHEP* **09** (2011) 045, [arXiv:1104.2846 \[hep-th\]](#).
- [34] J. Soda, H. Kodama, and M. Nozawa, “Parity Violation in Graviton Non-gaussianity,” *JHEP* **08** (2011) 067, [arXiv:1106.3228 \[hep-th\]](#).
- [35] M. Shiraishi, D. Nitta, and S. Yokoyama, “Parity Violation of Gravitons in the CMB Bispectrum,” *Prog. Theor. Phys.* **126** (2011) 937–959, [arXiv:1108.0175 \[astro-ph.CO\]](#).
- [36] A. Agrawal, T. Fujita, and E. Komatsu, “Large tensor non-Gaussianity from axion-gauge field dynamics,” *Phys. Rev. D* **97** no. 10, (2018) 103526, [arXiv:1707.03023 \[astro-ph.CO\]](#).
- [37] X. Gao, T. Kobayashi, M. Yamaguchi, and J. Yokoyama, “Primordial non-Gaussianities of gravitational waves in the most general single-field inflation model,” *Phys. Rev. Lett.* **107** (2011) 211301, [arXiv:1108.3513 \[astro-ph.CO\]](#).
- [38] L. Bordin, P. Creminelli, M. Mirbabayi, and J. Noreña, “Tensor Squeezed Limits and the Higuchi Bound,” *JCAP* **09** (2016) 041, [arXiv:1605.08424 \[astro-ph.CO\]](#).
- [39] N. Bartolo, V. Domcke, D. G. Figueroa, J. García-Bellido, M. Peloso, M. Pieroni, A. Ricciardone, M. Sakellariadou, L. Sorbo, and G. Tasinato, “Probing non-Gaussian Stochastic Gravitational Wave Backgrounds with LISA,” *JCAP* **11** (2018) 034, [arXiv:1806.02819 \[astro-ph.CO\]](#).
- [40] O. Ozsoy, M. Mylova, S. Parameswaran, C. Powell, G. Tasinato, and I. Zavala, “Squeezed tensor non-Gaussianity in non-attractor inflation,” *JCAP* **09** (2019) 036, [arXiv:1902.04976 \[hep-th\]](#).
- [41] V. De Luca, J. Khoury, and S. S. C. Wong, “Gravitational memory and Ward identities in the local detector frame,” *Phys. Rev. D* **112** no. 2, (2025) 024032, [arXiv:2412.12273 \[gr-qc\]](#).
- [42] R. Durrer, P. G. Ferreira, and T. Kahniashvili, “Tensor microwave anisotropies from a stochastic magnetic field,” *Phys. Rev. D* **61** (2000) 043001, [arXiv:astro-ph/9911040](#).
- [43] C. Caprini and R. Durrer, “Gravitational wave production: A Strong constraint on primordial magnetic fields,” *Phys. Rev. D* **65** (2001) 023517, [arXiv:astro-ph/0106244](#).
- [44] A. Mack, T. Kahniashvili, and A. Kosowsky, “Microwave background signatures of a primordial stochastic magnetic field,” *Phys. Rev. D* **65** (2002) 123004, [arXiv:astro-ph/0105504](#).
- [45] J. R. Shaw and A. Lewis, “Massive Neutrinos and Magnetic Fields in the Early Universe,” *Phys. Rev. D* **81** (2010) 043517, [arXiv:0911.2714 \[astro-ph.CO\]](#).
- [46] S. Saga, H. Tashiro, and S. Yokoyama, “Limits on primordial magnetic fields from direct detection experiments of gravitational wave background,” *Phys. Rev. D* **98** no. 8, (2018) 083518, [arXiv:1807.00561 \[astro-ph.CO\]](#).
- [47] O. Özsoy and G. Tasinato, “Vector dark matter, inflation, and non-minimal couplings with gravity,” *JCAP* **06** (2024) 003, [arXiv:2310.03862 \[astro-ph.CO\]](#).
- [48] A. Bhaumik, T. Papanikolaou, and A. Ghoshal, “Vector induced Gravitational Waves sourced by Primordial Magnetic Fields,” [arXiv:2504.10477 \[astro-ph.CO\]](#).

- [49] S. Maiti, D. Maity, and R. Srikanth, “Probing Reheating Phase via Non-Helical Magnetogenesis and Secondary Gravitational Waves,” [arXiv:2505.13623](#) [[astro-ph.CO](#)].
- [50] B. Atkins, D. Chowdhury, A. Marriott-Best, and G. Tasinato, “Inflationary magnetogenesis beyond slow-roll and its induced gravitational waves,” *Phys. Rev. D* **112** no. 6, (2025) 063534, [arXiv:2507.01772](#) [[astro-ph.CO](#)].
- [51] S. Matarrese, O. Pantano, and D. Saez, “General relativistic dynamics of irrotational dust: Cosmological implications,” *Phys. Rev. Lett.* **72** (1994) 320–323, [arXiv:astro-ph/9310036](#).
- [52] S. Matarrese, S. Mollerach, and M. Bruni, “Second order perturbations of the Einstein-de Sitter universe,” *Phys. Rev. D* **58** (1998) 043504, [arXiv:astro-ph/9707278](#).
- [53] K. N. Ananda, C. Clarkson, and D. Wands, “The Cosmological gravitational wave background from primordial density perturbations,” *Phys. Rev. D* **75** (2007) 123518, [arXiv:gr-qc/0612013](#).
- [54] D. Baumann, P. J. Steinhardt, K. Takahashi, and K. Ichiki, “Gravitational Wave Spectrum Induced by Primordial Scalar Perturbations,” *Phys. Rev. D* **76** (2007) 084019, [arXiv:hep-th/0703290](#).
- [55] R. Saito and J. Yokoyama, “Gravitational-Wave Constraints on the Abundance of Primordial Black Holes,” *Prog. Theor. Phys.* **123** (2010) 867–886, [arXiv:0912.5317](#) [[astro-ph.CO](#)]. [Erratum: *Prog.Theor.Phys.* 126, 351–352 (2011)].
- [56] J. R. Espinosa, D. Racco, and A. Riotto, “A Cosmological Signature of the SM Higgs Instability: Gravitational Waves,” *JCAP* **09** (2018) 012, [arXiv:1804.07732](#) [[hep-ph](#)].
- [57] K. Kohri and T. Terada, “Semianalytic calculation of gravitational wave spectrum nonlinearly induced from primordial curvature perturbations,” *Phys. Rev. D* **97** no. 12, (2018) 123532, [arXiv:1804.08577](#) [[gr-qc](#)].
- [58] C. Powell and G. Tasinato, “Probing a stationary non-Gaussian background of stochastic gravitational waves with pulsar timing arrays,” *JCAP* **01** (2020) 017, [arXiv:1910.04758](#) [[gr-qc](#)].
- [59] G. Tasinato, “Gravitational wave nonlinearities and pulsar-timing array angular correlations,” *Phys. Rev. D* **105** no. 8, (2022) 083506, [arXiv:2203.15440](#) [[gr-qc](#)].
- [60] N. M. Jiménez Cruz, F. C. Sánchez, and G. Tasinato, “New test of modified gravity with gravitational wave experiments,” [arXiv:2509.08273](#) [[gr-qc](#)].
- [61] P. W. Graham, J. Mardon, and S. Rajendran, “Vector Dark Matter from Inflationary Fluctuations,” *Phys. Rev. D* **93** no. 10, (2016) 103520, [arXiv:1504.02102](#) [[hep-ph](#)].
- [62] B. Ratra, “Cosmological ‘seed’ magnetic field from inflation,” *Astrophys. J. Lett.* **391** (1992) L1–L4.
- [63] H. V. Ragavendra, G. Tasinato, and L. Sriramkumar, “Chiral gravitational waves from multi-phase magnetogenesis,” [arXiv:2602.16575](#) [[astro-ph.CO](#)].
- [64] C. Caprini, R. Durrer, and T. Kahniashvili, “The Cosmic microwave background and helical magnetic fields: The Tensor mode,” *Phys. Rev. D* **69** (2004) 063006, [arXiv:astro-ph/0304556](#).
- [65] M. Maggiore, *Gravitational Waves. Vol. 2: Astrophysics and Cosmology*. Oxford University Press, 3, 2018.
- [66] A. Marriott-Best, M. Peloso, and G. Tasinato, “New gravitational wave probe of vector dark matter,” *Phys. Rev. D* **111** no. 10, (2025) 103511, [arXiv:2502.13116](#) [[astro-ph.CO](#)].
- [67] N. Bartolo, V. De Luca, G. Franciolini, M. Peloso, D. Racco, and A. Riotto, “Testing primordial black holes as dark matter with LISA,” *Phys. Rev. D* **99** no. 10, (2019) 103521, [arXiv:1810.12224](#) [[astro-ph.CO](#)].

- [68] N. Bartolo, V. De Luca, G. Franciolini, A. Lewis, M. Peloso, and A. Riotto, “Primordial Black Hole Dark Matter: LISA Serendipity,” *Phys. Rev. Lett.* **122** no. 21, (2019) 211301, [arXiv:1810.12218](#) [[astro-ph.CO](#)].
- [69] B. Allen, “Variance of the Hellings-Downs correlation,” *Phys. Rev. D* **107** no. 4, (2023) 043018, [arXiv:2205.05637](#) [[gr-qc](#)].
- [70] R. C. Bernardo and K.-W. Ng, “Pulsar and cosmic variances of pulsar timing-array correlation measurements of the stochastic gravitational wave background,” *JCAP* **11** (2022) 046, [arXiv:2209.14834](#) [[gr-qc](#)].
- [71] **NANOGrav** Collaboration, G. Agazie *et al.*, “The NANOGrav 15 yr Data Set: Evidence for a Gravitational-wave Background,” *Astrophys. J. Lett.* **951** no. 1, (2023) L8, [arXiv:2306.16213](#) [[astro-ph.HE](#)].
- [72] D. J. Reardon *et al.*, “Search for an Isotropic Gravitational-wave Background with the Parkes Pulsar Timing Array,” *Astrophys. J. Lett.* **951** no. 1, (2023) L6, [arXiv:2306.16215](#) [[astro-ph.HE](#)].
- [73] H. Xu *et al.*, “Searching for the Nano-Hertz Stochastic Gravitational Wave Background with the Chinese Pulsar Timing Array Data Release I,” *Res. Astron. Astrophys.* **23** no. 7, (2023) 075024, [arXiv:2306.16216](#) [[astro-ph.HE](#)].
- [74] **EPTA, InPTA:** Collaboration, J. Antoniadis *et al.*, “The second data release from the European Pulsar Timing Array - III. Search for gravitational wave signals,” *Astron. Astrophys.* **678** (2023) A50, [arXiv:2306.16214](#) [[astro-ph.HE](#)].
- [75] D. G. Figueroa, M. Pieroni, A. Ricciardone, and P. Simakachorn, “Cosmological Background Interpretation of Pulsar Timing Array Data,” *Phys. Rev. Lett.* **132** no. 17, (2024) 171002, [arXiv:2307.02399](#) [[astro-ph.CO](#)].
- [76] R. w. Hellings and G. s. Downs, “UPPER LIMITS ON THE ISOTROPIC GRAVITATIONAL RADIATION BACKGROUND FROM PULSAR TIMING ANALYSIS,” *Astrophys. J. Lett.* **265** (1983) L39–L42.
- [77] R. C. Bernardo and K.-W. Ng, “Charting the nanohertz gravitational wave sky with pulsar timing arrays,” *Int. J. Mod. Phys. D* **34** no. 04, (2025) 2540013, [arXiv:2409.07955](#) [[astro-ph.CO](#)].
- [78] J. D. Romano and B. Allen, “Answers to frequently asked questions about the pulsar timing array Hellings and Downs curve,” *Class. Quant. Grav.* **41** no. 17, (2024) 175008, [arXiv:2308.05847](#) [[gr-qc](#)].
- [79] B. Allen and J. D. Romano, “Hellings and Downs correlation of an arbitrary set of pulsars,” *Phys. Rev. D* **108** no. 4, (2023) 043026, [arXiv:2208.07230](#) [[gr-qc](#)].
- [80] R. C. Bernardo and K.-W. Ng, “Hunting the stochastic gravitational wave background in pulsar timing array cross correlations through theoretical uncertainty,” *JCAP* **08** (2023) 028, [arXiv:2304.07040](#) [[gr-qc](#)].
- [81] S. Valtolina, G. Shaifullah, A. Samajdar, and A. Sesana, “Testing strengths, limitations, and biases of current pulsar timing arrays’ detection analyses on realistic data,” *Astron. Astrophys.* **683** (2024) A201, [arXiv:2309.13117](#) [[astro-ph.HE](#)].
- [82] B. Allen and S. Valtolina, “Pulsar timing array source ensembles,” *Phys. Rev. D* **109** no. 8, (2024) 083038, [arXiv:2401.14329](#) [[gr-qc](#)].
- [83] N. Grimm, M. Pijenburg, G. Cusin, and C. Bonvin, “The impact of large-scale galaxy clustering on the variance of the Hellings-Downs correlation: theoretical framework,” *JCAP* **03** (2025) 011, [arXiv:2404.05670](#) [[astro-ph.CO](#)].

- [84] D. Agarwal and J. D. Romano, “Cosmic variance of the Hellings and Downs correlation for ensembles of universes having nonzero angular power spectra,” *Phys. Rev. D* **110** no. 4, (2024) 043044, [arXiv:2404.08574 \[gr-qc\]](#).
- [85] W. G. Lamb and S. R. Taylor, “Spectral Variance in a Stochastic Gravitational-wave Background from a Binary Population,” *Astrophys. J. Lett.* **971** no. 1, (2024) L10, [arXiv:2407.06270 \[gr-qc\]](#).
- [86] Y.-M. Wu, Y.-C. Bi, and Q.-G. Huang, “Spatial correlations between pulsars for interfering gravitational-wave sources in pulsar timing array,” *Phys. Rev. D* **112** no. 12, (2025) 123034, [arXiv:2407.07319 \[astro-ph.CO\]](#).
- [87] C. Pitrou and G. Cusin, “Mitigating cosmic variance in the Hellings-Downs curve: A cosmic microwave background analogy,” *Phys. Rev. D* **111** no. 8, (2025) 083544, [arXiv:2412.12073 \[gr-qc\]](#).
- [88] V. Domcke, G. Franciolini, and M. Pieroni, “Cosmic Variance in Anisotropy Searches at Pulsar Timing Arrays,” [arXiv:2508.21131 \[astro-ph.CO\]](#).
- [89] **LIGO Scientific** Collaboration, J. Aasi *et al.*, “Advanced LIGO,” *Class. Quant. Grav.* **32** (2015) 074001, [arXiv:1411.4547 \[gr-qc\]](#).
- [90] **VIRGO** Collaboration, F. Acernese *et al.*, “Advanced Virgo: a second-generation interferometric gravitational wave detector,” *Class. Quant. Grav.* **32** no. 2, (2015) 024001, [arXiv:1408.3978 \[gr-qc\]](#).
- [91] **KAGRA** Collaboration, Y. Aso, Y. Michimura, K. Somiya, M. Ando, O. Miyakawa, T. Sekiguchi, D. Tatsumi, and H. Yamamoto, “Interferometer design of the KAGRA gravitational wave detector,” *Phys. Rev. D* **88** no. 4, (2013) 043007, [arXiv:1306.6747 \[gr-qc\]](#).
- [92] **ET** Collaboration, A. Abac *et al.*, “The Science of the Einstein Telescope,” [arXiv:2503.12263 \[gr-qc\]](#).
- [93] B. Allen and J. D. Romano, “Detecting a stochastic background of gravitational radiation: Signal processing strategies and sensitivities,” *Phys. Rev. D* **59** (1999) 102001, [arXiv:gr-qc/9710117](#).